

Topology and shape optimization of 3D prestressed concrete structures

Emad Shakur^{1a}, Adaya Shaked^b, Oded Amir^b

^aRICAM – Johann Radon Institute for Computational and Applied Mathematics, Altenbergerstraße 69, Linz, 4040, Austria

^bTechnion – Israel Institute of Technology, Technion City, Haifa, 3200003, Israel

Abstract

In this paper we introduce a computational framework for optimizing 3D prestressed concrete structures. The procedure combines shape optimization of post-tensioning cables with topology optimization of concrete, enabling novel design configurations of 3D beams and plates. Prestressing cables are modeled as B-spline curves that are embedded within a concrete continuum and whose control points serve as design variables. Concurrently, the distribution of concrete is determined by density-based topology optimization. A special filter enforces concrete cover around the cables, creating a coupling between the two sets of design variables. The optimization problem formulation mimics the design intent of prestressed concrete structures, separating the load-balancing part with respect to permanent loads from stiffness maximization with respect to live loads. Results show that material savings exceeding 30% can be achieved compared to solid prestressed members, strengthening the argument in favor of using prestressed concrete for reducing embodied CO₂. The complete implementation in MATLAB is provided as supplementary material.

Keywords: topology optimization, shape optimization, prestressed concrete, embodied CO₂

1. Introduction

Prestressed concrete is used extensively in new infrastructure, e.g. road and railway bridges, as well as in buildings with relatively large spans. The use of prestressing steel increases the durability of concrete structures due to the reduction, or even elimination, of tensile stresses. Prestressing also reduces the sizes of concrete members that are utilized more efficiently than their reinforced concrete counterparts, providing an economic advantage as well as the capability to design for larger spans.

Optimization of concrete structures, and prestressed ones in particular, is gaining interest for two main reasons. One is the significant contribution of cement production to global CO₂ emissions (Andrew, 2019). Prestressed concrete structures have an advantage w.r.t. embodied CO₂ (Miller et al., 2015; Broyles and Hopper, 2023) and formal optimization can further reduce the quantities of raw materials and hence also the embodied CO₂. Another motivation for optimizing prestressed concrete is the growing interest in 3D concrete printing, with prestressing being one of the methods that is being explored for joining printed parts and resisting bending (Vantighem et al., 2020; Ooms et al., 2022; Li et al., 2024).

These motivations call for formulating and developing shape and topology optimization procedures that are tailored specifically for prestressed concrete. The challenge is that the shape of the prestressing cables and the topology of the concrete structure need to be optimized simultaneously. The cables transfer equivalent forces to the concrete, that depend on the shape and should counteract external loads – indicating a coupling between shape and topology. Moreover, in most practical scenarios, the cables are covered by concrete – indicating another coupling between shape and topology.

Simultaneous shape and topology optimization of prestressed structures is a relatively new research topic. It was approached by Amir and Shakour (2018a) where 2D beams were optimized for stiffness, with a single cable that was parameterized by a set of linear segments. Later, the prestressing force was added as a design parameter to be minimized and B-splines were employed for modeling the cable, allowing to impose curvature constraints (Amir and Shakour, 2018b). More recently, Zhang et al. (2021) reformulated the design parameterization using spline bases for the cable and the continuum concrete, and introduced stress constraints which are necessary in realistic applications. Another related work presented topology optimization of concrete girders with prestressed shape memory alloys, that hold the advantage of applying local prestressing effects (Sung and Andrawes, 2023). Finally, Jha and Pathak (2023) presented concurrent shape optimization of a concrete beam and its post-tensioning cable. The authors considered also frictional losses which have not been accounted for in previous studies.

In the current work, we present a framework for optimizing 3D concrete structures with 3D post-tensioning cables. The purpose is to allow complete design freedom in 3D that can generate innovative design concepts. Our formulation enables direct design of 3D beams, eliminating manual interpretation of 2D optimization (Vantighem et al., 2020; Ooms et al., 2022). Another exciting application is the optimization of post-tensioned plates, where research has shown that optimal cable layouts are curved in 3D (e.g., Sarkisian et al., 2018; Zelickman and Amir, 2021) and the interaction with topology optimization of concrete has yet to be explored.

The remainder of the article is organized as follows. Modeling and design parametrization of both concrete and prestressing steel are described in Section 2. The

optimization problem and subsequent sensitivity analysis are presented in Sections 3 and 4. Several design examples are presented and discussed in Section 5 and concluding remarks are provided in Section 6.

2. Modeling and design parameterization

In this section, we present the methodology adopted in the current paper for modeling prestressed concrete elements and provide details on their design parameterization. The prestressed elements are modeled as a 3D continuum discretized using tri-linear cube finite elements, with embedded cables that are parameterized by B-splines. The optimization is formulated to simultaneously optimize the topology of the concrete, that is controlled by pseudo-density design variables (Bendsøe, 1989; Bendsøe and Sigmund, 2003), and the shape of the cables, that is determined by the splines' control points.

Specifically, we use quadratic B-spline curves

$$\mathbf{C}(\xi) = \sum_{i=1}^{N_{cp}} \mathbf{P}_i N_{i,2}(\xi)$$

where $\mathbf{C}(\xi)$ is the quadratic three-dimensional B-spline curve; ξ is the parameter along the curve; \mathbf{P}_i and $N_{i,2}(\xi)$ represent the control point i of the curve and its corresponding quadratic B-spline basis function, respectively; and N_{cp} is the number of control points. All the B-splines curves in this paper are defined over open uniform knot vectors. The spatial coordinates of the curve's control points serve as shape design variables in the optimization problem. An illustration of a continuum domain with a single embedded cable is depicted in Figure 1.

2.1. Pseudo-density representation

The density design variables in this paper are subjected to three consecutive filters to prevent numerical instabilities (Sigmund and Petersson, 1998) and meet specific geometrical requirements. The first is a density filter (Bruns and Tortorelli, 2001; Bourdin, 2001) which is formulated as a PDE (Lazarov and Sigmund, 2011). In its discretized form, we solve

$$\left(l_o^2 \mathbf{K}_f + \mathbf{M}_f^{\text{vol}} + l_s \mathbf{M}_f^{\text{surf}} \right) \tilde{\rho} = \mathbf{T}\rho \quad (1)$$

where ρ is the vector of density design variables; $\tilde{\rho}$ is the vector of their filtered values; l_o is the bulk length scale parameter that is related to the traditional filter radius r_{\min} ; and l_s is the surface length scale parameter that guarantees consistent filtering on the boundaries (Wallin et al., 2020). Further details on the implementation of Eq. (1) and the finite element assembly of \mathbf{K}_f , $\mathbf{M}_f^{\text{vol}}$, $\mathbf{M}_f^{\text{surf}}$ and \mathbf{T} can be found in Lazarov and Sigmund (2011); Wallin et al. (2020). In the current context, we impose $l_s = l_o$ on faces whose material distribution is free, and $l_s = 0$ on faces that either contain prescribed solids or belong to symmetry planes. As commonly done in topology optimization procedures, Eq. (1) is formulated based on the same finite element discretization that is used for solving the displacements.

The second filter is applied to ensure an adequate concrete cover for the prestressing cables. In the majority of

applications involving prestressed elements, it is essential for the prestressing cables to be fully embedded within the concrete. In the numerical model, this is materialized by ensuring that the B-spline curve representing the cable is covered by finite elements with solid material. For this purpose, we adopt the filter suggested in Amir and Shakour (2018a,b) and extend it to accommodate 3D designs. In the remainder of this paper, we refer to this filter as the cable-to-concrete filter. By applying the filter, concrete elements located within a specified radius around the cable are pushed to the material phase using a super-Gaussian function. The influence region of this filter is illustrated in Figure 2.

The cable-to-concrete filter is applied to the filtered densities $\tilde{\rho}$, while each $\tilde{\rho}_i$ is updated as follows,

$$\hat{\rho}_i = \tilde{\rho}_i + (1 - \tilde{\rho}_i) e^{-\frac{1}{2} \left(\frac{d_i}{r_{cf}} \right)^\mu} \quad (2)$$

where $\hat{\rho}_i$ represents the modified density of concrete element i ; d_i is the minimal distance between the concrete element i and a cable segment; r_{cf} is the radius of the cable-to-concrete filter; and μ represents the sharpness of the super-Gaussian function. Notice that this filter couples the density and shape design variables through the distance d_i . While the control points representing the cables are adjusted, the distance changes, affecting the resulting filtered densities. A plot of the super-Gaussian function with respect to the distance d_i , for $\tilde{\rho} = 0.5$, $r_{cf} = 4$, and various values of μ is displayed in Figure 3a. As the sharpness parameter μ increases, the region surrounding the cable becomes more crisply defined. Notice that when the distance is below r_{cf} , the density is pushed to 1, while when the distance is greater than r_{cf} , the density tends to remain the same. For further demonstration of the effect of the filter, a plot for different values of $\tilde{\rho}$ is presented in Figure 3b and an illustration of a 2D cross-section of a cable with its surrounding elements is presented in Figure 4.

Finally, to ensure a clear separation between the void and material regions, the densities $\hat{\rho}$ are subjected to a smooth Heaviside projection function (Guest et al., 2004; Xu et al., 2010). Specifically, this projection is formulated following the 'robust' topology optimization formulation (Wang et al., 2011; Lazarov et al., 2016) that allows to consider worst-case scenarios. Herein, we employ the eroded layout for stiffness evaluation and the dilated layout for volume evaluation, even though our stiffness measure is not strictly a compliance functional hence the eroded layout is not strictly the worst case. The element-level eroded and dilated densities are defined as (Wang et al., 2011)

$$\bar{\rho}^{\text{ero}} = \frac{\tanh(\beta_{HS}\eta_{\text{ero}}) + \tanh(\beta_{HS}(\hat{\rho}_i - \eta_{\text{ero}}))}{\tanh(\beta_{HS}\eta_{\text{ero}}) + \tanh(\beta_{HS}(1 - \eta_{\text{ero}}))} \quad (3)$$

$$\bar{\rho}_i^{\text{dil}} = \frac{\tanh(\beta_{HS}\eta_{\text{dil}}) + \tanh(\beta_{HS}(\hat{\rho}_i - \eta_{\text{dil}}))}{\tanh(\beta_{HS}\eta_{\text{dil}}) + \tanh(\beta_{HS}(1 - \eta_{\text{dil}}))} \quad (4)$$

where β_{HS} governs the sharpness of the smooth projection; η_{ero} is the projection threshold for the eroded layout (e.g., $\eta_{\text{ero}} = 0.6$); and η_{dil} is the projection threshold for the dilated layout (e.g., $\eta_{\text{dil}} = 0.4$). The intermediate layout, with $\bar{\rho}^{\text{int}}$ which is considered as the actual design intended

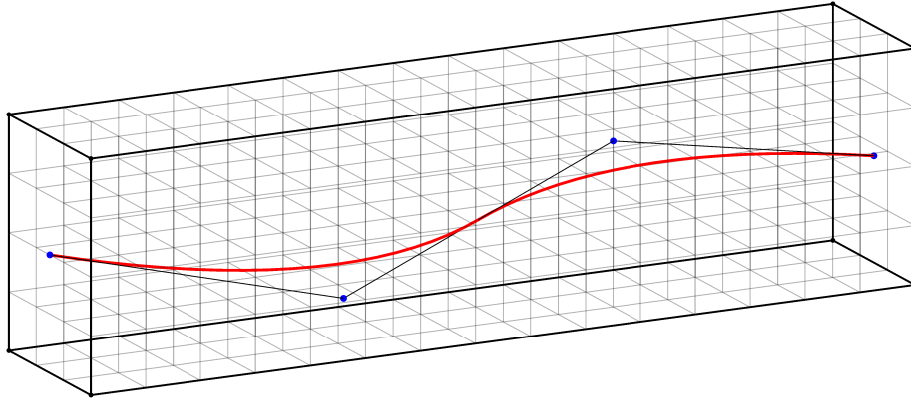


Figure 1: An illustrative model of a continuum domain with a single embedded cable. The cable shape is outlined in red, its four control points are marked by blue dots and the control polygon is outlined by a black polyline.

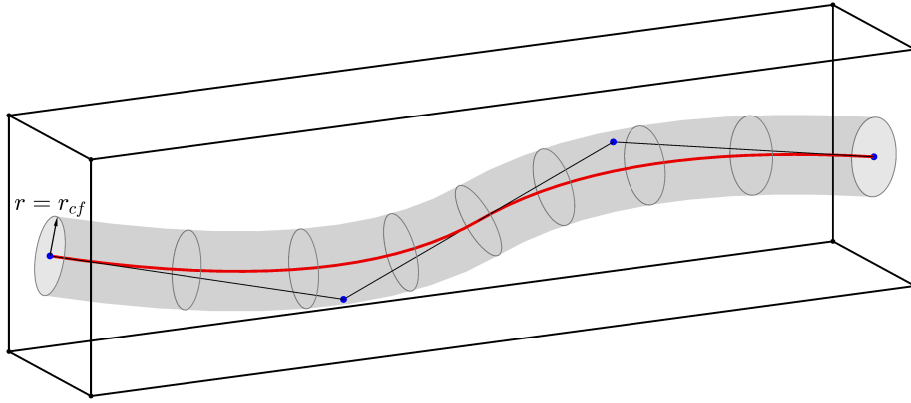


Figure 2: The influence region of the cable-to-concrete filter.

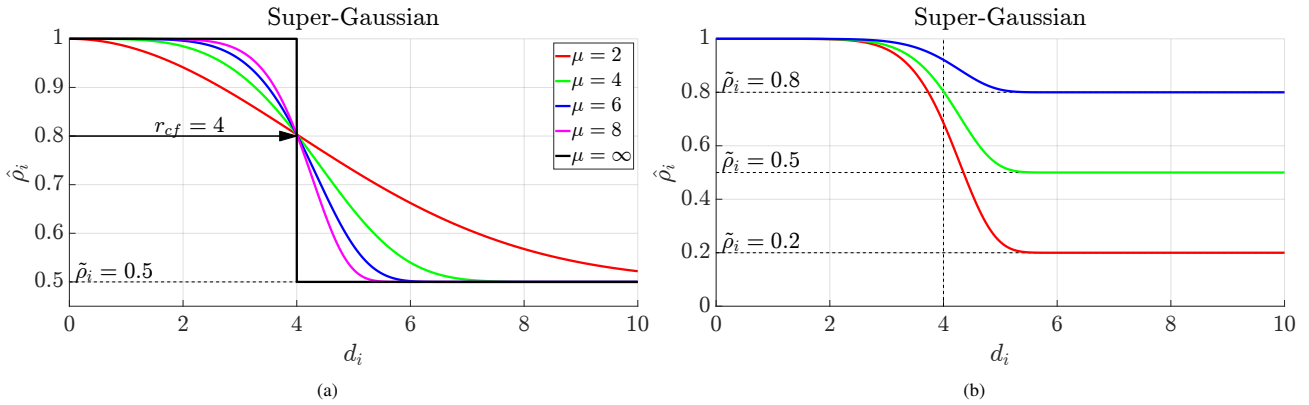


Figure 3: The super-Gaussian function used for the cable-to-concrete filter. Left: $\tilde{\rho} = 0.5$, $r_{cf} = 4$ and different values of μ ; Right: $r_{cf} = 4$, $\mu = 8$ and different values of $\tilde{\rho}$.

for manufacturing, is evaluated similarly using $\eta_{\text{int}} = 0.5$. We note that the response according to this layout does not need to be evaluated during the optimization. However, the volume of this layout is evaluated to adjust the volume constraint, as will be discussed in Section 5.

After implementing all filters, the structural response is evaluated over the eroded layout with $\bar{\rho}_{\text{ero}}$, where the Young's modulus of each concrete element is determined by a Modified SIMP interpolation scheme (Sigmund and Torquato, 1997),

$$E_i(\bar{\rho}_i^{\text{ero}}) = E_{\min} + (E_{\max} - E_{\min}) (\bar{\rho}_i^{\text{ero}})^{p_E} \quad (5)$$

where E_{\min} is a relatively small positive number in order

to avoid singularity of the stiffness matrix; E_{\max} is the actual value of Young's modulus for concrete; and p_E is a penalization factor that drives the design towards a 0-1 distribution.

2.2. Prestressing forces

The prestressed elements in this paper are subjected to four different forces: prestressing forces, self-weight, external dead loads and external live loads. The nodal force vectors associated with these forces are denoted as \mathbf{f}_p , \mathbf{f}_s , \mathbf{f}_d , and \mathbf{f}_l , respectively. Dead and live loads are applied to the prestressed structural elements in specified regions based on the problem settings. The self-weight is

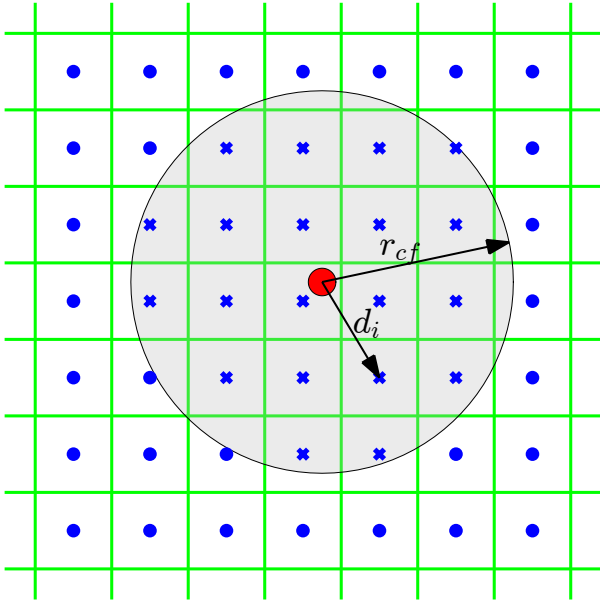


Figure 4: An illustration of a 2D cross-section of a cable with its surrounding elements. Concrete elements that should be pushed to the material phase are marked with blue crosses, while elements that should not be affected are marked with blue dots.

evaluated according to the eroded layout while the weight of each finite element is applied to its associated degrees of freedom. For a specific finite element i , the local nodal force vector due to self-weight is evaluated as follows,

$$\mathbf{f}_{s,i} = \gamma_c v_i \bar{\rho}_i^{\text{ero}} \mathbf{N}_i,$$

where γ_c is the specific weight of concrete; v_i is the volume of the finite element; and \mathbf{N}_i represents the shape functions of the finite element.

The prestressing forces are modeled as distributed forces acting along the cable in its normal direction due to the cable's curvature, as well as point loads at the anchorages. These forces are denoted as $\mathbf{F}_p^{\text{Curv}}$ and $\mathbf{F}_p^{\text{Anc}}$, respectively. A demonstration of is presented in Figure 5. To evaluate the forces and subsequently compute the prestressing nodal force vector \mathbf{f}_p , the following steps are performed:

1. The intersections of the cable with the finite element grid are found. Thanks to the second-order B-spline representation of the cable, the intersection points can be determined analytically with ξ being the unknown variable. Specifically, we solve the equations $x(\xi) = x_{\text{Grid}}$, $y(\xi) = y_{\text{Grid}}$, and $z(\xi) = z_{\text{Grid}}$ to find the intersection points with the $y-z$, $x-z$, and $x-y$ planes, respectively.
2. For each cable segment between two intersection points, $\mathbf{F}_p^{\text{Curv}}$ is defined:

$$\mathbf{F}_p^{\text{Curv}}(\xi) = T_p \tilde{\kappa} \hat{\mathbf{n}},$$

where $\tilde{\kappa}$ is the average curvature between the two intersection points, $\tilde{\kappa} = (\kappa(\xi_s) + \kappa(\xi_e))/2$; ξ_s and ξ_e are the values of ξ at the intersection points; T_p is the prestressing force in the cable; and $\hat{\mathbf{n}}$ is the normal vector of the cable. The curvature and the normal vector as a function of ξ are evaluated as follows,

$$\kappa(\xi) = \frac{|\mathbf{C}' \times \mathbf{C}''|}{|\mathbf{C}'|^3}$$

and

$$\hat{\mathbf{n}}(\xi) = \frac{\mathbf{C}' \times (\mathbf{C}'' \times \mathbf{C}')}{|\mathbf{C}'| |\mathbf{C}'' \times \mathbf{C}'|}.$$

A demonstration of $\mathbf{F}_p^{\text{Curv}}$ within a single finite element is presented in Figure 6.

3. Within each finite element, the force, $\mathbf{F}_p^{\text{Curv}}$, is projected to the finite element's nodes using the element's shape functions \mathbf{N}_i ,

$$\mathbf{f}_{p,i}^{\text{Curv}} = \int_{\xi_s}^{\xi_e} \mathbf{F}_p^{\text{Curv}} \mathbf{N}_i J d\xi$$

with $J(\xi)$ representing the Jacobian of the curve which is calculated by

$$J(\xi) = \sqrt{x(\xi)^2 + y(\xi)^2 + z(\xi)^2}$$

and \mathbf{N} with respect to ξ is defined as, $\mathbf{N}_i(\xi) = \mathbf{N}_i(\mathbf{C}) = \mathbf{N}_i(x(\xi), y(\xi), z(\xi))$.

4. The loads at the anchors are applied as point loads at the cable's ends. These loads are equal to the prestressing force and act in the direction tangential to the cable,

$$\mathbf{F}_p^{\text{Anc}}(\xi_{\text{ends}}) = T_p \mathbf{t}(\xi_{\text{ends}}),$$

where \mathbf{t} is the tangential direction of the cable and can be evaluated by $\mathbf{C}'/|\mathbf{C}'|$. Subsequently, the nodal prestressing forces at hosting elements of the cable's endpoints are evaluated by

$$\mathbf{f}_{p,i}^{\text{Anc}} = \mathbf{F}_p^{\text{Anc}} \mathbf{N}_i.$$

5. Finally, the prestressing force vector \mathbf{f}_p is assembled as follows,

$$\mathbf{f}_p = \sum_{i=1}^{N_E} (\mathbf{f}_{p,i}^{\text{Anc}} + \mathbf{f}_{p,i}^{\text{Curv}})$$

where N_E is the number of finite elements.

To facilitate the subsequent presentation and discussions regarding displacements, we denote the displacements caused by \mathbf{f}_p , \mathbf{f}_s , \mathbf{f}_d , and \mathbf{f}_l as \mathbf{u}_p , \mathbf{u}_s , \mathbf{u}_d , and \mathbf{u}_l , respectively. Additionally, the combined displacements resulting from multiple forces are represented by combining their subscripts. For instance, the displacements due to $\mathbf{f}_s + \mathbf{f}_d$ are denoted as \mathbf{u}_{sd} and the displacements arising from $\mathbf{f}_s + \mathbf{f}_d + \mathbf{f}_p$ are denoted as \mathbf{u}_{sdp} .

We note that the stiffness of the cable and force losses along the cable are neglected. Nevertheless, the formulation is capable of accommodating immediate losses resulting from friction, anchorage slip and elastic shortening, given their explicit dependence on the prestressing force, the curvature of the cable and concrete deformation. Furthermore, long-term losses due to creep, shrinkage, and relaxation can be evaluated based on cable forces and concrete deformation, and can be incorporated into the computation of prestressing forces.

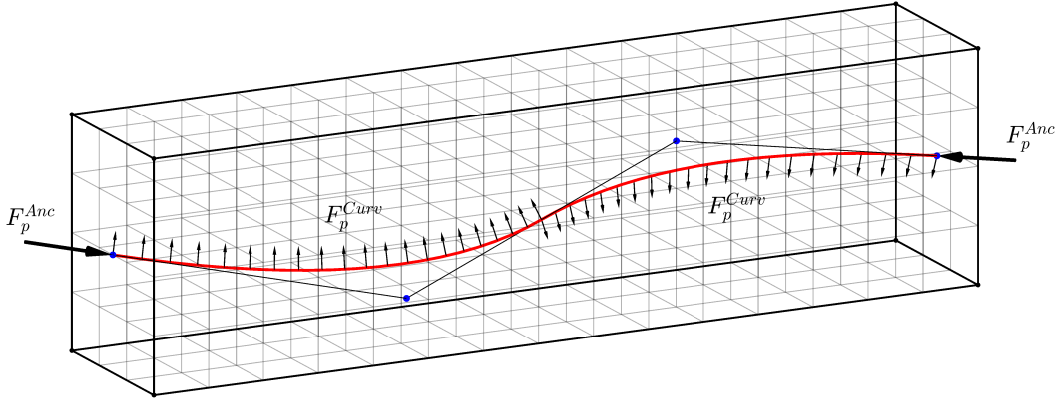


Figure 5: A demonstration of the prestressing forces acting on a three-dimensional beam model. $\mathbf{F}_p^{\text{Curv}}$ represents the prestressing forces due to the curvature of the cable while F_p^{Anc} represents the prestressing forces at the anchors.

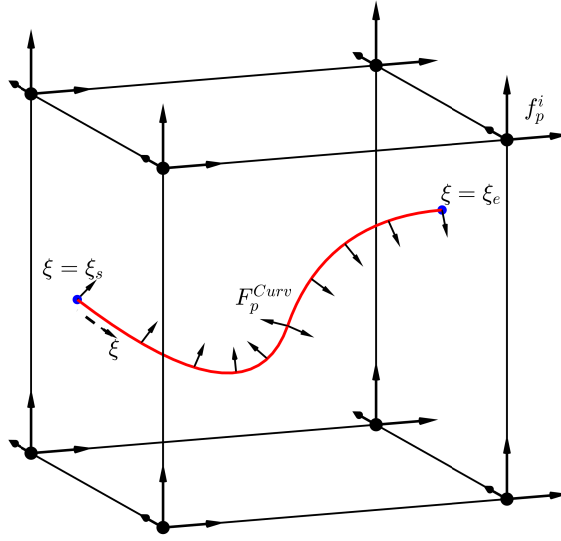


Figure 6: A demonstration of $\mathbf{F}_p^{\text{Curv}}$ within a single finite element. The blue dots indicate intersection points between the cable and the finite element.

3. Problem formulation

The optimization problem is formulated to simultaneously optimize the topology of concrete and the shape of the embedded cables. The topology is optimized following the density-based approach (Bendsøe, 1989; Bendsøe and Sigmund, 2003). The shape optimization is simultaneously conducted by adjusting the positions of the B-splines' control points. The objective of the optimization involves minimizing compliance and displacement-related terms, while limiting the amount of concrete in the optimized design.

The objective function in this paper has been uniquely developed to incorporate a commonly adopted concept in the design of prestressed elements. In prestressed concrete design, the prestressing forces balance the structural response due to self-weight and permanent dead loads, while live loads are subsequently applied to the already-balanced design. To align with this concept, we formulate the objective function to minimize two separate measures.

The first part of the objective is defined as

$$\phi_1 = (\mathbf{1} \circ \mathbf{u}_{sdp})^T (\mathbf{1} \circ \mathbf{u}_{sdp}), \quad (6)$$

and aims at minimizing the absolute displacements due to self-weight, permanent dead loads and prestressing – hence achieving a balanced structural response. In Eq. (6), the displacements to be balanced are designated by the degrees of freedom indicated by the vector $\mathbf{1}$ and the symbol \circ indicates component-wise multiplication. Typically, $\mathbf{1}$ will refer to the primary loading surface of the structure, where also the live loads are applied. Without loss of generality, herein the vector $\mathbf{1}$ corresponds to vertical DOF in the top surface of the prestressed structure.

The second part of the objective is defined as

$$\phi_2 = \mathbf{f}_l^T \mathbf{u}_l$$

and aims at minimizing the compliance due to live loads. The key difference between the two parts of the objective is that ϕ_2 drives the concrete's topology towards the stiffest design under live loads, while ϕ_1 is not directly related to stiffness. By minimizing ϕ_1 , the design should accommodate several sets of loads and reach a neutral displacement field. Previous work has shown that when the prestressing force is too large, the topology adapts itself by softening parts of the structure to reach neutral displacements (Amir and Shakour, 2018a). One way to avoid this phe-

nomenon is to minimize also the prestressing force (Amir and Shakour, 2018b). Herein, we choose to minimize two separate measures, a choice which is aligned with practical preliminary design of prestressed structures. At the same time, a reasonable value for the prestressing force is determined prior to the optimization. We note that in principle, one can choose to apply only a certain portion of the dead loads in ϕ_1 and allow upwards deflections, and subsequently add the remainder of the dead loads to ϕ_2 . This depends on design preferences and various choices can be accommodated.

Mathematically, the simultaneous topology-shape optimization is formulated as follows,

$$\begin{aligned} \min_{[\rho, \mathbf{X}]} \quad & \tilde{\phi} = \frac{w_1}{\phi_1^0} \underbrace{(\mathbf{1} \circ \mathbf{u}_{sdp})^T (\mathbf{1} \circ \mathbf{u}_{sdp})}_{\phi_1} + \frac{w_2}{\phi_2^0} \underbrace{\mathbf{f}_l^T \mathbf{u}_l}_{\phi_2} \\ \text{s.t.} \quad & g = V(\bar{\rho}_{\text{dil}}) - V_{\text{dil}}^* \leq 0 \\ & 0 \leq \rho_e \leq 1, \quad e = 1, \dots, N_E \\ & \underline{\mathbf{X}} \leq \mathbf{X} \leq \bar{\mathbf{X}} \\ \text{with} \quad & \mathbf{K}_{\text{ero}} \mathbf{u}_{sdp} = \mathbf{f}_s + \mathbf{f}_d + \mathbf{f}_p \\ & \mathbf{K}_{\text{ero}} \mathbf{u}_l = \mathbf{f}_l \end{aligned} \quad (7)$$

where ρ is the vector of density design variables that determine the concrete's distribution; \mathbf{X} is the vector of shape design variables that determine the location of control points defining the cables, with lower and upper bounds $\underline{\mathbf{X}}$ and $\bar{\mathbf{X}}$, respectively; w_1 and w_2 are coefficients that provide proper weighting for each part of the objective; ϕ_1^0 and ϕ_2^0 are values of ϕ_1 and ϕ_2 at the initial design, used for scaling; N_E is the number of continuum finite elements, which is also the number of density design variables; $\bar{\rho}_{\text{dil}}$ is the projected dilated density used for imposing the volume constraint on the concrete, related to the mathematical variables ρ and \mathbf{X} via Eqs. (1),(2) and (4); V_{dil}^* is the allowable volume fraction for the concrete in its dilated configuration; and \mathbf{K}_{ero} is the stiffness matrix of the eroded concrete domain, assembled with $\bar{\rho}_{\text{ero}}$, which is related to the mathematical variables via Eqs. (1),(2) and (3).

We note that $\bar{\rho}_{\text{ero}}$ is used to evaluate both parts of the objective. For ϕ_2 , this is a straightforward choice because for compliance subject to a volume constraint, $\bar{\rho}_{\text{ero}}$ represents the worst case for compliance and $\bar{\rho}_{\text{dil}}$ the worst case for volume (Wang et al., 2016). Then we maintain $\bar{\rho}_{\text{ero}}$ also for evaluating ϕ_1 for the sake of consistency – meaning, the same structural configuration should be used to evaluate both measures – even though it is not necessarily a worst case for ϕ_1 , which is not a compliance measure.

4. Sensitivity analysis

In this section, we present the sensitivity analysis of the optimization problem introduced in Eq. (7). This problem exhibits coupling between the topology and shape design variables due to the cable-to-concrete filter: the density of the concrete surrounding the cable depends on the cable's shape variables. This coupling should be carefully accounted for in the sensitivity analysis. While we describe herein only the main steps needed for deriving the sensitivities, complete details and the numerical implementation

can be found in the MATLAB code that is provided as supplementary material.

We start by presenting the sensitivity analysis with respect to a generic design variable α . Then, we develop the specific derivatives with respect to the topological and shape design variables, ρ and \mathbf{X} , taking into account the coupling between them.

To differentiate the objective function, and to eliminate the implicit derivatives of the displacement fields \mathbf{u}_{sdp} and \mathbf{u}_l with respect to the design variables, we employ the adjoint method. The augmented objective functional is as follows,

$$\hat{\phi} = \frac{w_1}{\phi_1^0} (\mathbf{1} \circ \mathbf{u}_{sdp})^T (\mathbf{1} \circ \mathbf{u}_{sdp}) + \frac{w_2}{\phi_2^0} \mathbf{f}_l^T \mathbf{u}_l + \lambda_1^T (\mathbf{K}_{\text{ero}} \mathbf{u}_{sdp} - \mathbf{f}_s - \mathbf{f}_d - \mathbf{f}_p) + \lambda_2^T (\mathbf{K}_{\text{ero}} \mathbf{u}_l - \mathbf{f}_l) \quad (8)$$

where λ_1 and λ_2 are the adjoint vectors. The derivative of Eq. (8) w.r.t. α is

$$\begin{aligned} \frac{d\hat{\phi}}{d\alpha} = & 2 \frac{w_1}{\phi_1^0} (\mathbf{1} \circ \mathbf{u}_{sdp})^T \mathbf{1} \circ \left(\frac{\partial \mathbf{u}_{sdp}}{\partial \alpha} \right) + \frac{w_2}{\phi_2^0} \mathbf{f}_l^T \frac{\partial \mathbf{u}_l}{\partial \alpha} \\ & + \lambda_1^T \left(\frac{\partial \mathbf{K}_{\text{ero}}}{\partial \alpha} \mathbf{u}_{sdp} + \mathbf{K}_{\text{ero}} \frac{\partial \mathbf{u}_{sdp}}{\partial \alpha} - \frac{\partial \mathbf{f}_s}{\partial \alpha} - \frac{\partial \mathbf{f}_p}{\partial \alpha} \right) \\ & + \lambda_2^T \left(\frac{\partial \mathbf{K}_{\text{ero}}}{\partial \alpha} \mathbf{u}_l + \mathbf{K}_{\text{ero}} \frac{\partial \mathbf{u}_l}{\partial \alpha} \right) \end{aligned} \quad (9)$$

where we assume that the dead and live loads do not depend on the design variable α .

To eliminate the dependence on $\frac{\partial \mathbf{u}_{sdp}}{\partial \alpha}$, we gather all relevant terms as follows,

$$2 \frac{w_1}{\phi_1^0} (\mathbf{1} \circ \mathbf{u}_{sdp})^T \mathbf{1} \circ \frac{\partial \mathbf{u}_{sdp}}{\partial \alpha} + \lambda_1^T \mathbf{K}_{\text{ero}} \frac{\partial \mathbf{u}_{sdp}}{\partial \alpha} = 0,$$

leading to the first adjoint equation

$$\mathbf{K}_{\text{ero}}^T \lambda_1 = -2 \frac{w_1}{\phi_1^0} (\mathbf{1} \circ \mathbf{u}_{sdp} \circ \mathbf{1}).$$

Similarly, to eliminate the dependence on $\frac{\partial \mathbf{u}_l}{\partial \alpha}$, we gather all relevant terms and obtain the second adjoint equation

$$\mathbf{K}_{\text{ero}}^T \lambda_2 = -\frac{w_2}{\phi_2^0} \mathbf{f}_l$$

that reflects the fact that the second term of the objective is essentially self-adjoint and we can use

$$\lambda_2 = -\frac{w_2}{\phi_2^0} \mathbf{u}_l. \quad (10)$$

Once the adjoint vectors are obtained, they can be substituted back into Eq (9), yielding final sensitivities that contain only explicit derivatives. We note that in this equation, \mathbf{K}_{ero} and \mathbf{f}_s can be represented as functions solely of the densities in the eroded layout, $\mathbf{K}_{\text{ero}}(\bar{\rho}^{\text{ero}}(\rho, \mathbf{X}))$ and $\mathbf{f}_s(\bar{\rho}^{\text{ero}}(\rho, \mathbf{X}))$. Their dependence on the topology and shape design variables ρ and \mathbf{X} is established through the three consecutive filters. Additionally, we note that \mathbf{f}_p depends only on the shape design variables, $\mathbf{f}_p(\mathbf{X})$. Representing $\hat{\phi}$ as $\hat{\phi}(\bar{\rho}^{\text{ero}}(\rho, \mathbf{X}), \mathbf{X})$, its explicit derivatives w.r.t the density and shape design variables are

$$\frac{d\hat{\phi}}{d\rho} = \frac{\partial \hat{\phi}}{\partial \bar{\rho}^{\text{ero}}} \frac{\partial \bar{\rho}^{\text{ero}}}{\partial \rho} \quad \text{and} \quad \frac{\partial \hat{\phi}}{\partial \mathbf{X}} = \frac{\partial \hat{\phi}}{\partial \bar{\rho}^{\text{ero}}} \frac{\partial \bar{\rho}^{\text{ero}}}{\partial \mathbf{X}} + \frac{\partial \hat{\phi}}{\partial \mathbf{X}} \quad (11)$$

$$\frac{d\hat{\phi}}{d\mathbf{X}} = \frac{\partial\hat{\phi}}{\partial\bar{\rho}^{\text{ero}}} \frac{\partial\bar{\rho}^{\text{ero}}}{\partial\hat{\rho}} \frac{\partial\hat{\rho}}{\partial\mathbf{X}} + \frac{\partial\hat{\phi}}{\partial\mathbf{X}}, \quad (12)$$

respectively, where

$$\frac{\partial\hat{\phi}}{\partial\bar{\rho}^{\text{ero}}} = \lambda_1^T \left(\frac{\partial\mathbf{K}_{\text{ero}}}{\partial\bar{\rho}^{\text{ero}}} \mathbf{u}_{sdp} - \frac{\partial\mathbf{f}_s}{\partial\bar{\rho}^{\text{ero}}} \right) - \frac{w_2}{\phi_2^0} \mathbf{u}_l^T \frac{\partial\mathbf{K}_{\text{ero}}}{\partial\bar{\rho}^{\text{ero}}} \mathbf{u}_l, \quad (13)$$

$$\frac{\partial\hat{\phi}}{\partial\mathbf{X}} = -\lambda_1 \frac{\partial\mathbf{f}_p}{\partial\mathbf{X}}. \quad (14)$$

The components in Eqs. (11) to (14) are evaluated explicitly through the following relations:

- $\frac{\partial\mathbf{K}_{\text{ero}}}{\partial\bar{\rho}^{\text{ero}}}$ is related to the interpolation rule (5) for the stiffness;
- $\frac{\partial\bar{\rho}^{\text{ero}}}{\partial\hat{\rho}}$ is related to the smooth Heaviside projection (3);
- $\frac{\partial\hat{\rho}}{\partial\bar{\rho}}$ is related to the cable-to-concrete filter (2);
- $\frac{\partial\tilde{\rho}}{\partial\bar{\rho}}$ is the derivative of the PDE filter (1).

Regarding the derivatives of the force vectors, the derivative of the prestressing forces $\frac{\partial\mathbf{f}_p}{\partial\mathbf{X}}$ is evaluated by differentiating the procedure and geometrical relations for constructing \mathbf{f}_p , as presented in Section 2. The derivative of the self-weight force vector, $\frac{\partial\mathbf{f}_s}{\partial\bar{\rho}^{\text{ero}}}$, is straightforward and can be computed according to the corresponding expression provided in Section 2.

Regarding the volume constraint, as the dilated volume of the design is a function of the dilated densities, $V(\bar{\rho}^{\text{dil}})$, its derivatives w.r.t to the topology and shape design variables are:

$$\frac{dg}{d\bar{\rho}} = \frac{\partial g}{\partial\bar{\rho}^{\text{dil}}} \frac{\partial\bar{\rho}^{\text{dil}}}{\partial\hat{\rho}} \frac{\partial\hat{\rho}}{\partial\bar{\rho}} \frac{\partial\tilde{\rho}}{\partial\bar{\rho}}, \quad (15)$$

$$\frac{dg}{d\mathbf{X}} = \frac{\partial g}{\partial\bar{\rho}^{\text{dil}}} \frac{\partial\bar{\rho}^{\text{dil}}}{\partial\hat{\rho}} \frac{\partial\hat{\rho}}{\partial\mathbf{X}}. \quad (16)$$

5. Examples

In this section, we demonstrate and investigate the capability of the suggested approach to achieve simultaneous optimization of the cable shape and the concrete topology in 3D prestressed structures. We present four different examples. In the first two examples, we showcase the design of prestressed beams, with single and multi-span configurations. The third and fourth examples address the design of prestressed slabs with different boundary conditions.

All physical measures, material properties, and loads in the following examples are chosen to resemble practical scenarios. The material properties are set to $E_{\text{max}} = 3 \cdot 10^7 \text{ kN/m}^2$, $E_{\text{min}} = 1 \cdot 10^{-3} \text{ kN/m}^2$ and $\nu = 0.2$. For computing the self-weight, the specific weight of concrete is set to 25 kN/m^3 . The SIMP penalty is set to $p_E = 3$ in all examples. The Heaviside projection functions are computed with $\eta_{\text{dil}} = 0.4$ and $\eta_{\text{ero}} = 0.6$. To control the sharpness of the Heaviside projection, the sharpness

parameter β_{HS} begins at 1 and is multiplied by 2 every 20 iterations, up to a maximum value of 8. The sharpness parameter of the cable-to-concrete filter is kept fixed at $\mu = 2$ during all optimization iterations. All other parameters are problem-specific and are explicitly stated in the respective examples. The allowable volume of the dilated design, V_{dil}^* , as defined in Eq. (7), is initially set to the allowable volume of the intermediate design, denoted by V_{int}^* . This value is adjusted continuously during the optimization to ensure that the volume of the intermediate design ultimately aligns with its allowable volume fraction. This adjustment is performed using the formula: $V_{\text{dil}}^* = (V(\bar{\rho}^{\text{dil}}) \cdot V_{\text{int}}^*) / V(\bar{\rho}^{\text{int}})$.

For optimization in the nested approach, we employ the Method of Moving Asymptotes – MMA (Svanberg, 1987). The optimization terminates when the absolute change in the objective and the constraint between consecutive iterations is less than a certain threshold for three consecutive iterations. This threshold is set to 10^{-4} for the beam examples and 10^{-3} for the slab examples, reflecting the increased number of design variables. A minimum number of 60 iterations is set to ensure the sharpness parameter β_{HS} reaches its maximal value, and the maximum number of iterations is set to 100.

To impose clear concrete cover, the maximal values of the shape design variables are set to ensure that the corresponding cable stays within a distance of 0.05 m from the boundaries of the design domain. The move limits on the density design variables are set to 0.2, while the move limits on the shape design variables are specified in each example because they depend on the domain size. In all examples, the objective weights are set to $w_1 = w_2 = 0.5$. To ensure force transfer of dead and live loads, two layers of finite elements are prescribed as concrete material on the upper surfaces where loads are applied. The vector \mathbf{l} in Eq. (6) is constructed to activate all the vertical displacements in the top surfaces.

Each cable in Examples 1, 3, and 4 is represented using six control points. In the test cases for Example 2, the cable is represented using eight control points, due to the longer prestressed elements. All the cables are defined by open uniform knot vectors. To ensure the cable is perpendicular to the symmetry surfaces, the shape design variables of the two consecutive control points near the symmetry surface are adjusted and then merged so that they align with the normal direction of the symmetry surfaces. For example, if the cable intersects a symmetry surface whose normal is in the x -direction, the y - and z -coordinates of the crossing control point and the one before are set to be identical, and then merged into a single design variable for each direction. In general, because a straight cable does not create transverse forces due to its zero curvature, we impose a small perturbation of the control points in the initial design. This prevents the commencement of optimization without meaningful sensitivity information.

5.1. Simply supported beam

In this example, we demonstrate the design of a simply supported beam, subjected to uniformly distributed external loads. The beam domain has a length-to-height ratio of $15 : 1$ with a span of 12 m and a cross-section

of $0.4 \text{ m} \times 0.8 \text{ m}$. The dead and live loads are both set to 30 kN/m , distributed uniformly over the upper chord of the beam. Utilizing the symmetry of the problem, we model and optimize only the quarter-symmetric part. The model is discretized with cube finite elements of size 0.025 m , resulting in a grid composed of $240 \times 8 \times 32$ finite elements. The setup of the numerical model is presented in Figure 7. Note that vertical supports are distributed along the entire height of the beam. If a single support was placed at the beam’s bottom corner, the optimization process would require additional material to create a vertical connection between the support and the anchoring point of the cable.

The prestressing force in the cable is set to balance the external dead load with half of the self-weight of the beam domain distributed over its upper chord, $q = 30 + \frac{25 \cdot 0.4 \cdot 0.8}{2} = 34 \text{ kN/m}$. For this purpose, the cable is assumed to be parabolic with zero eccentricity at the beam’s ends and an eccentricity of $e_{max} = 0.35 \text{ m}$ in mid-span. The balancing force is then set to

$$T_p = \frac{ql^2}{8e_{max}} = 1748 \text{ kN}. \quad (17)$$

Note that since only the quarter-symmetric part is being modeled, only half of the prestressing force and the external loads are applied in the numerical model.

The allowable volume fraction of concrete in the intermediate phase is limited to 50%. The radii of the density filter, r_{min} , and the cable-to-concrete filter, r_{cf} , are both set to 0.1 m . The design comprises a single prestressing cable and we optimize only the vertical coordinates of the control points. The move limit for these coordinates is set to 0.05 m with maximal and minimal values set to 0.05 m and 0.75 m , respectively, leading to a minimal distance of 0.05 m from the lower and the upper chords of the beam. The coordinates in the longitudinal direction are equally spaced along the beam and remain fixed during the optimization process. Due to symmetry, the cable is positioned at the central plane of the beam and is fixed in the transverse direction during the optimization.

The initial design is depicted in Figure 8. This design is achieved by setting all the density design variables to 0.5 and placing the vertical coordinates defining the cable at the mid-height of the beam. Filtered intermediate densities exceeding a value of 0.75 are highlighted in the figure. The figure clearly illustrates the influence region of the cable-to-concrete filter, where the densities of the elements within the specified filter radius are pushed to their material phase. The optimization terminated after 71 iterations, yielding the optimized design presented in Figure 9. We summarize the values for various measures in both the initial and final designs in Table 1.

Convergence of the optimization is portrayed in Figure 10, indicating the stability of the optimization procedure. As the optimization progresses, the load-balancing component of the objective $w_1 \phi_1 / \phi_1^0$ gradually converges towards zero with a value of $8.2e-4$ in the optimized design, leading to the final objective being nearly equal to the compliance component. This can also be observed in Table 1, where their values are recorded as 0.127 and 0.128. The

graph illustrates also the convergence of the volume constraint, g , represented in magenta. The minor fluctuations in the 20th and 40th iterations correspond to adjustments made to the sharpness parameters β_{HS} at those iterations.

Measure	Initial design	Final design
$\phi_1 [m^2]$	6.321	0.010
$\phi_2 [kNm]$	5.181	1.319
$w_1 \phi_1 / \phi_1^0 [-]$	0.5	$8.2e-4$
$w_2 \phi_2 / \phi_2^0 [-]$	0.5	0.127
$\tilde{\phi} [-]$	1	0.128
$V_{int} [m^3]$	0.561	0.480
$g [m^3]$	0.104	$-3.1e-5$

Table 1: Optimization of a simply supported beam. Summary of the values for various measures in the initial and final designs.

To further examine the optimization, specifically its effect on the deflection of the beam, we measure the vertical displacement of the beam at mid-span due to various combinations of forces. For this purpose we use the eroded domain which was used for evaluating displacements during optimization. The displacements corresponding to the initial and final designs are summarized in Table 2, and the evolution during the optimization is illustrated in Figure 11. As expected, the displacement due to self-weight and dead loads, u_{sd} , is balanced by the displacement due to prestressing, u_p , with their total sum being 0.001 m . We note that since the dead and live loads are equal, the difference between the magenta and red lines in the figure is, in fact, the displacement due to self-weight.

Next, we verify the balancing effect in the intermediate layout. We note that in this configuration, the beam exhibits a slightly higher stiffness and a minor increase in self-weight. This does not have a significant effect on the displacements at the examination point, with $u_{sdp} = 0.001$ and $u_{sdpl} = -0.020$ in the intermediate layout. Therefore, given these small differences in the response across the different layouts, we consider that the balance is preserved in the intermediate layout, even though the eroded layout was utilized for optimization. Additionally, the ratio between the maximal displacement u_{sdpl} in the intermediate layout and the span length is $0.02/12 = 1/600$. Considering that the permanent loads are roughly balanced, it is expected that the long-term deflection will be acceptable according to design requirements. Nevertheless, the examples herein merely demonstrate the potential of the method, and we do not attempt to provide a detailed assessment of the long-term deflection.

Design	u_{sd}^{mid}	u_p^{mid}	u_{sdp}^{mid}	u_l^{mid}	u_{sdpl}^{mid}
Initial	-0.093	0.034	-0.058	-0.081	-0.140
Final	-0.026	0.027	0.001	-0.023	-0.022

Table 2: Displacements at mid-span of the beam due to different combinations of forces, measured in meters.

It is interesting to observe the displacements along the upper chord of the beam resulting from the permanent loads in the final design, as shown in Figure 12. The plot exposes the interplay between the displacements due to dead loads and self-weight with those due to prestressing.

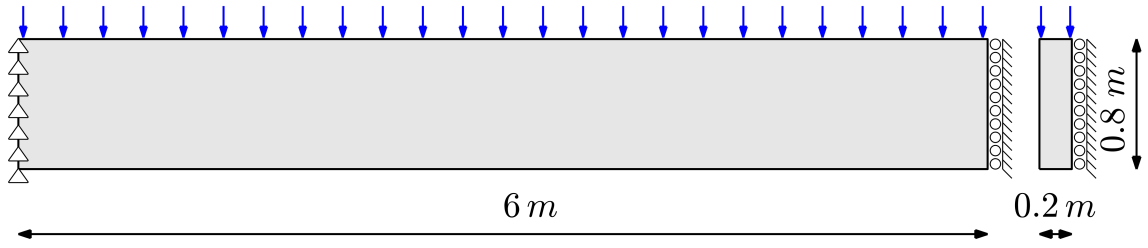


Figure 7: Problem setup for a quarter-symmetric part of the simply supported beam.

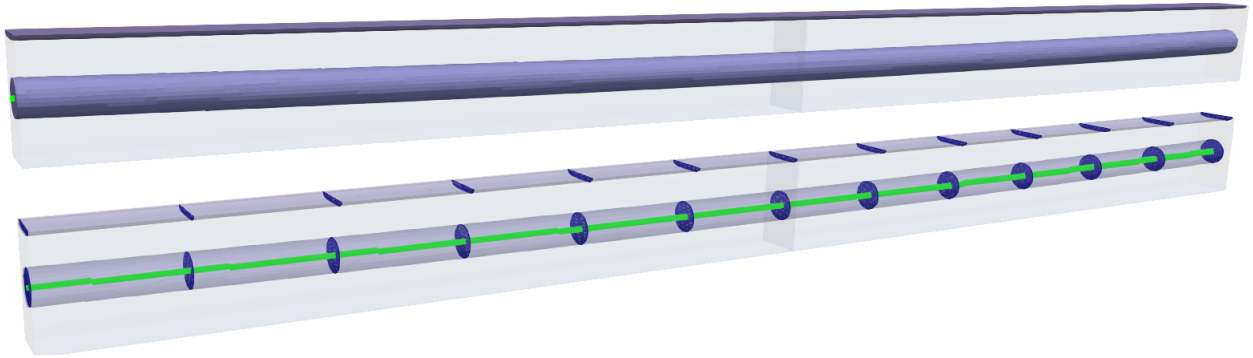


Figure 8: Initial design of the simply supported beam. Top: Original design. Bottom: Transparent view, revealing the cable's shape and cross sections every 1 meter along the beam.

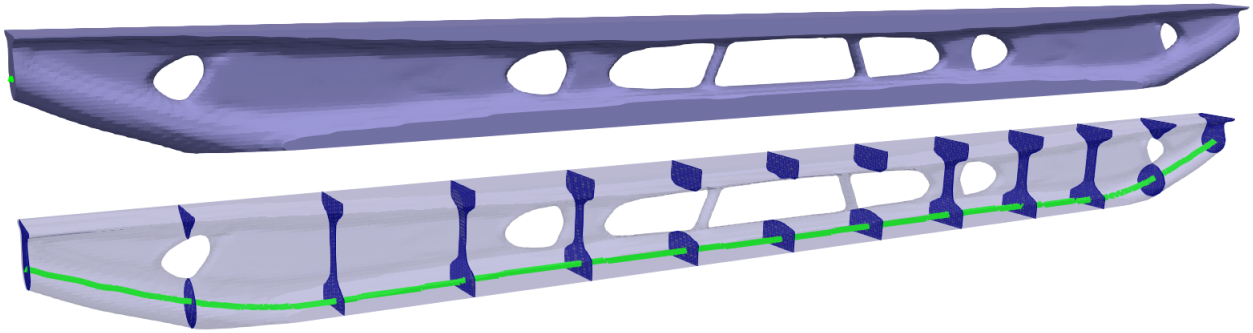


Figure 9: Optimized design of the simply supported beam. Top: Original design. Bottom: Transparent view, revealing the cable's shape and cross sections every 1 meter along the beam.

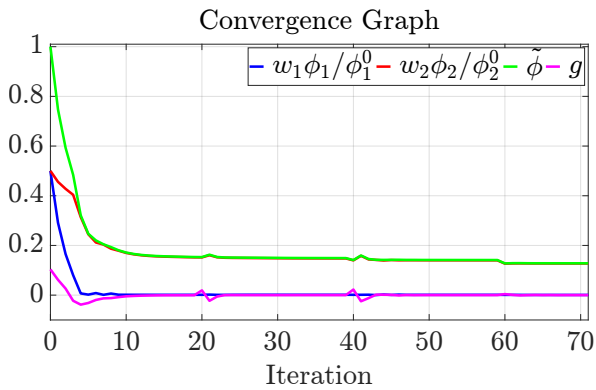


Figure 10: Convergence of the optimization problem, simply supported beam.

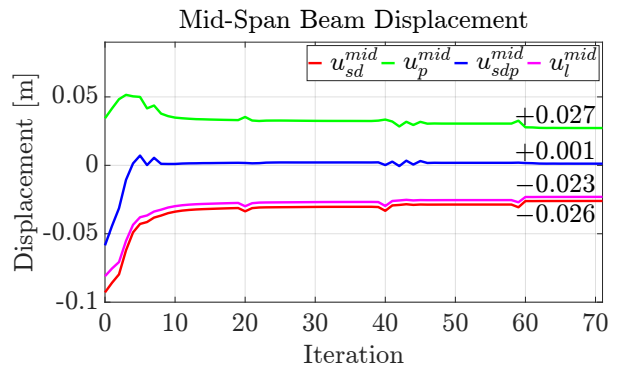


Figure 11: Convergence of vertical displacements at mid-span, simply supported beam.

The maximum combined displacement is 0.003 m , which does not occur at mid-span as typically happens in uniform beams. The maximum displacement occurs in close

proximity to the anchorage points, primarily influenced by the inclination of the anchor, the relatively high curvature of the cable and the reduced beam height in this region.

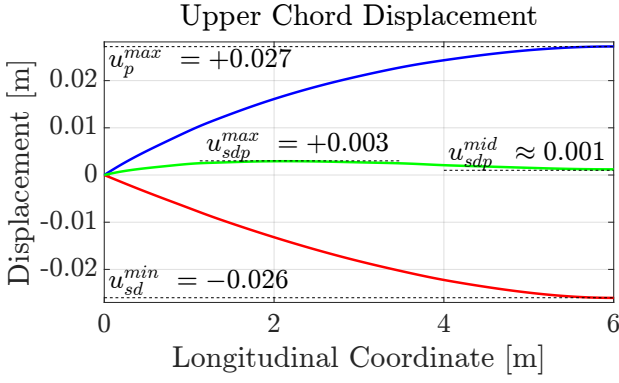


Figure 12: Displacements along the upper chord of the beam due to permanent loads (only symmetric half is presented).

The optimized design of Figure 9 can be used to evaluate the potential material savings achieved by the simultaneous topology and shape optimization. For this purpose, we find the depth of a solid beam that has the same compliance under live loads – i.e., the same ϕ_2 . Then, we find the prestressing force that balances the permanent loads, assuming a simple parabolic cable shape. The required depth of the beam is found to be slightly above 0.7 m and the prestressing force is 2220 kN. This reflects savings of 43% in concrete volume and 21% in prestressing force, while the design domain is enlarged by 0.1 m in the vertical direction. The reduction in prestressing force is a result of both the reduction in concrete weight and a certain increase of the maximum eccentricity.

We conclude this example by presenting optimized designs for the same problem settings but with different allowable volume fractions Vf_{int}^* for the intermediate layout. The optimized designs, along with the maximal displacement at mid-span and the final compliance, are presented in Figure 13. In all designs, balanced displacements due to permanent loads are obtained ($w_1\phi_1/\phi_1^0 < 0.001$), leading to an optimized objective that consists primarily of the compliance part. As expected, as the volume decreases, the compliance and the displacement at the examination point increase. Additionally, we illustrate the cables' shapes obtained for the different optimized designs in Figure 14. This illustration indicates that with an increased Vf_{int}^* , the cable exhibits reduced curvature. This emanates from the fact that higher Vf_{int}^* values lead to stiffer designs, requiring lower equivalent forces to achieve load balancing. Consequently, to control the equivalent forces, the optimization decreased cable curvature. Additionally, this illustration shows that in the stiffer designs obtained from higher Vf_{int}^* values, the cable shows slight curvature upwards, resulting in prestressing forces that act downwards. This may indicate that the combination of the prescribed prestressing force and the maximum eccentricity is too large, and the prestressing force could be reduced. Adding the minimization of prestressing force is possible (Amir and Shakour, 2018b) but was not pursued in the current work.

5.2. Multi-spans beam

In this section, we demonstrate the applicability of the proposed approach to the design of multi-span beams with

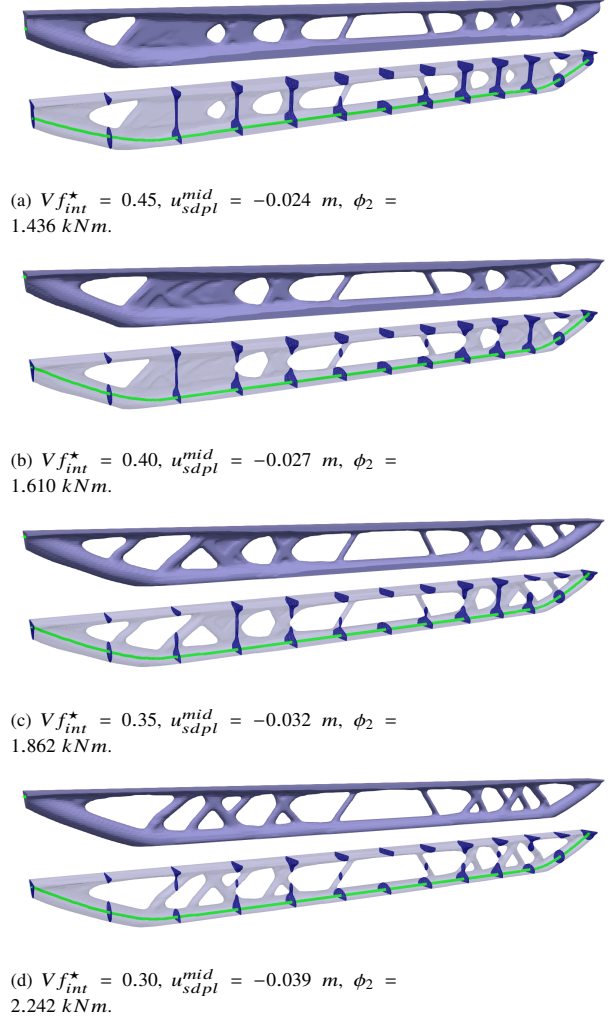


Figure 13: Optimized designs for various volume fractions Vf_{int}^* . The total vertical displacement at mid-span and the external compliance are depicted for each design.

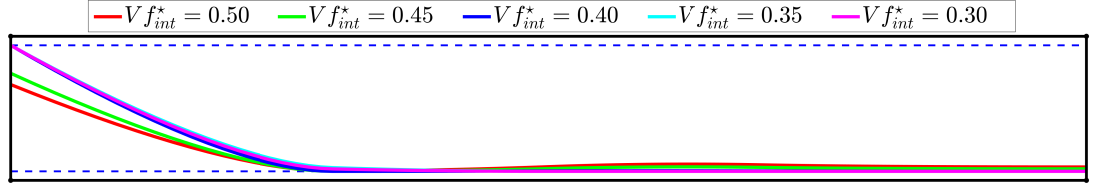


Figure 14: Optimized cable shapes for various volume fractions $V_{f_{int}}^*$, corresponding to the optimized designs in Figures 9 and 13. The dashed lines represent the upper and lower values of the shape design variables. Only the symmetric part of the beam is shown.

various setups. All design parameters remain consistent with those in the previous example. The changes involve the beam's length, boundary conditions, and prestressing force. Additionally, to account for the increased length of the beams compared to the previous example, we represent the prestressing cables using 8 control points instead of 6. Utilizing symmetry, we model and optimize only the quarter-symmetric parts of the beams. The volume fraction for the test cases is 50%.

The three test cases considered are: a two-span beam, a two-span beam with cantilevers, and a three-span beam. The span lengths and boundary conditions for these cases are depicted in Figure 15. With similar cross-section dimensions as in the previous example, the grid over the cross-section comprises 8×32 finite elements. Meanwhile, the grid size in the longitudinal direction varies according to the model, being 360, 440, and 540 for the three different cases, respectively. The prestressing forces are smaller than in to the previous example because of the shorter spans. For the first two cases, the prestressing force T_p is set to 300 kN, while in the third case, it is set to 500 kN. (150 kN and 250 kN in the quarter symmetric numerical models.) The optimization process for the three cases converges smoothly after 70, 66, and 68 iterations, respectively. Figure 16 presents the optimized designs with supports depicted as gray cones. We summarize the values for various measures in both the initial and final designs associated with these cases in Table 3.

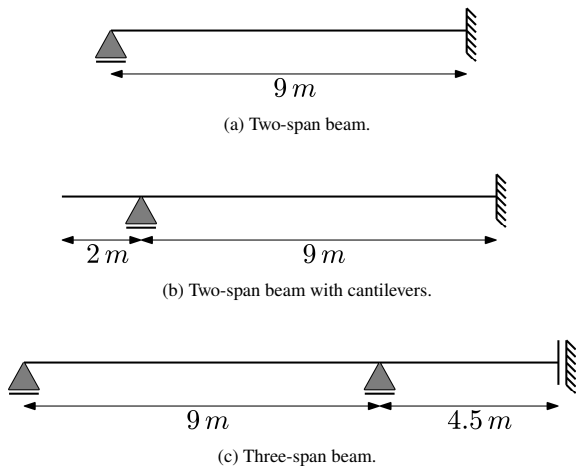


Figure 15: The three different settings for the numerical models of the multi-span beams.

In the three different cases, we can see similar behavior as before, with the displacement balancing part of the

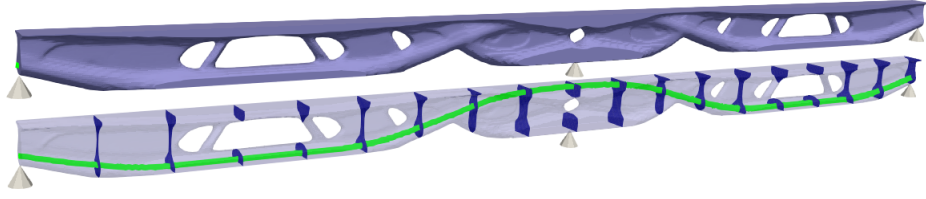
objective gradually diminishing, indicating that the desired displacement balance is approached in the optimized design. In all cases, the volume constraint is fulfilled. Additionally, the cables follow an expected path, being located at the upper chord of the beam in the internal support regions and in cantilevers, and at the lower chord in the spans.

5.3. Simply supported slab

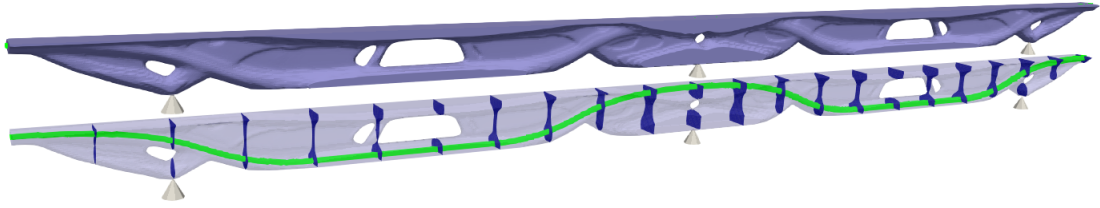
In this example, we use the proposed approach to optimize a simply supported prestressed slab. The design domain of the slab has dimensions of 12.8×12.8 m with a thickness of 0.32 m and it is subjected to uniformly distributed dead and live loads, each amounting to 10 kN/m². Exploiting double symmetry of the domain, we model only its quarter-symmetric part. The computational model is discretized with cube elements of size 0.04 m, resulting in a mesh of $160 \times 160 \times 8$ elements. Additionally, to exploit the symmetry about the diagonal of the numerical model, shape and topology design variables from one triangle are merged with their symmetric counterparts, resulting in a single set of design variables that determine the shape and topology of both parts. This symmetry cannot be exploited for the analysis due to the use of cube finite elements. Therefore, for analysis, the entire mesh of the numerical model is employed. The problem settings of the numerical model are illustrated in Figure 17.

The allowable volume fraction of concrete in the intermediate phase is limited to 50%. The radii of the density filter, r_{min} , and the cable-to-concrete filter, r_{cf} , are both set to 0.12 m. The prestressing force is set to $T_p = 1400$ kN. This value was chosen based on preliminary results of similar test cases where the formulation included also the prestressing force as a design variable (Shaked, 2023). The design consists of four cables in each planar direction, hence two cables in each planar direction in the numerical model. During optimization, specific coordinates of the cables are kept constant. For cables with initial geometry aligned with the x -direction, the x -coordinates of their control points are kept constant, while the y and z (vertical) coordinates are optimized. The same concept is applied to cables whose initial geometry is aligned with the y -direction. The design domain for each optimized coordinate is set to be at a distance of 0.05 m from the slab ends. The move limits on the shape design variables in this example are set to 0.3 m in the planar direction and 0.1 m in the vertical direction of the slab.

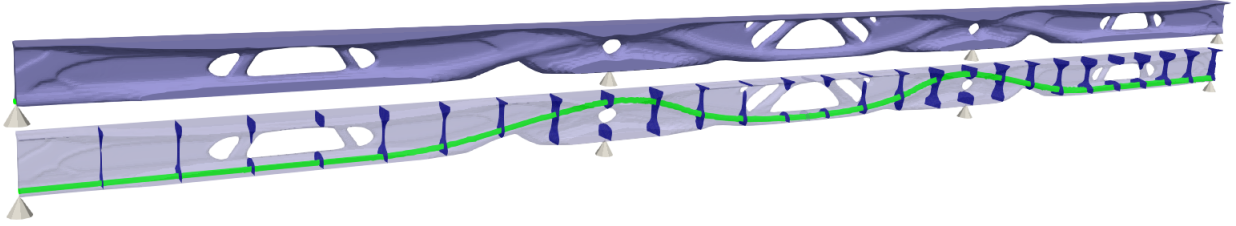
The initial design is depicted in Figure 18a, with the initial density design variable values set to 0.5. In this



(a) Two-span beam.



(b) Two-span beam with cantilevers.



(c) Three-span beam.

Figure 16: Optimized designs for the multi-span beams. Original designs and transparent views revealing the cables' shapes and cross-sections at 1-meter intervals along the beam.

Measure	Two-span beam		Two-span beam + cantilevers		Three-span beam	
	Initial design	Final design	Initial design	Final design	Initial design	Final design
$\phi_1 [m^2]$	0.270	0.004	0.200	0.001	0.424	0.001
$\phi_2 [kNm]$	0.974	0.272	0.732	0.196	1.312	0.359
$w_1\phi_1/\phi_1^0 [-]$	0.5	0.008	0.5	0.004	0.5	0.002
$w_2\phi_2/\phi_2^0 [-]$	0.5	0.140	0.5	0.134	0.5	0.137
$\tilde{\phi} [-]$	1	0.147	1	0.138	1	0.138
$V_{int} [m^3]$	0.841	0.720	1.028	0.880	1.262	1.080
$g [m^3]$	0.104	$-2.2e-5$	0.104	$-7.0e-6$	0.104	$-3.4e-6$

Table 3: Optimization of multi-span beams. Summary of the values for various measures in the initial and final designs.

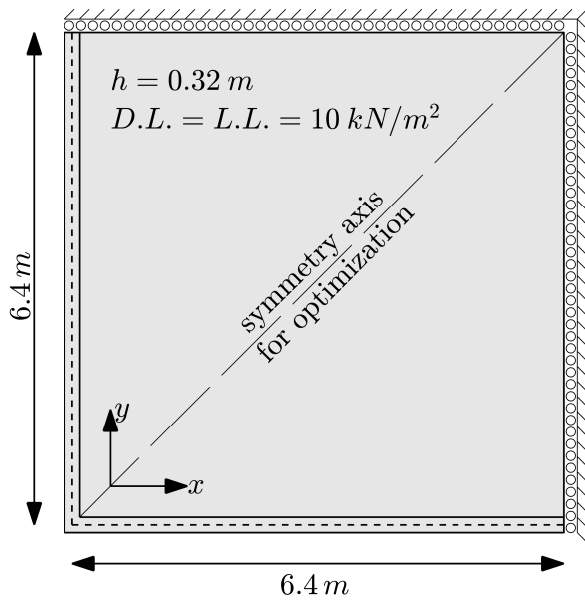


Figure 17: Problem setup for a quarter-symmetric part of the simply supported slab.

design, the distance between the cables in each direction is 3.2 m with a 1.6 m distance from the slab ends. All cables are positioned at the mid-plane of the slab. The optimization is terminated after 68 iterations, yielding the optimized design shown in Figure 18b. A planar view of the optimized design from the bottom is presented in Figure 19. In this design, all the cables are pushed to their minimal allowed height of 0.05 m and are fully embedded in the concrete. The optimized topology includes a prescribed material layer with thickness of 0.08 m at the upper surface of the slab. Additionally, the optimization created regions of material at the bottom surface of the slab with an average thickness of 0.08 m . In the optimized design, material regions from the upper and lower parts of the slab are interconnected by diagonal column-like parts, curved beam-like regions that cover the cables, and straight beam-like sections near the corners of the slab. This is illustrated in Figure 20 that shows the slicing of the design at the mid-plane, exposing the connections between its upper and lower parts.

In Figure 21 we present the planar configurations of the cables in the initial and optimized designs. The cables are marked with four distinct colors while each cable and its symmetric counterpart are marked with the same color. As seen in Figure 21b, the cable configuration forms a circle-like shape with a radius of 2.55 m at the center of the slab. Since all the cables are positioned at the bottom of the design domain in the vertical direction, this arrangement creates a compression ring in the bottom part of the slab. As the displacement field resulting from prestressing is influenced by the general configuration of the cables, this compression ring is interpreted as a specialized treatment designed to counterbalance the expected maximum displacement at the center of the slab, which arises due to dead load and self-weight. A possible explanation for the circular prestressing is its axis-symmetric effect on the vertical displacements. We presume that such axis-symmetric prestressing provides more effective load

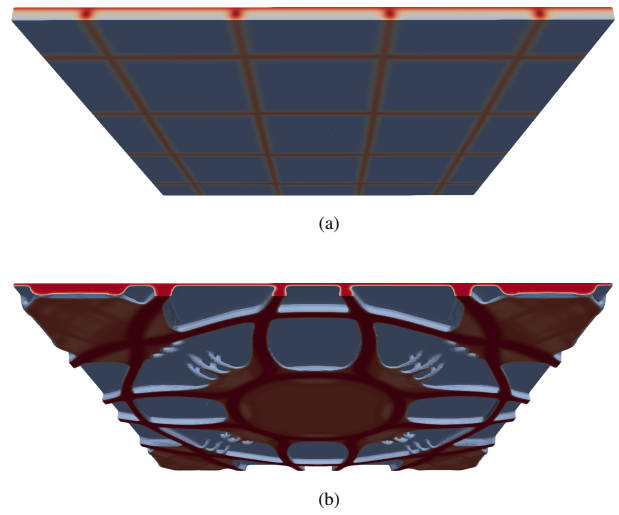


Figure 18: Initial and optimized designs of the simply supported slab. (a) Initial design with intermediate densities ranging from 0 (blue) to 1 (red). (b) Final design with intermediate densities ranging from 0.5 to 1.

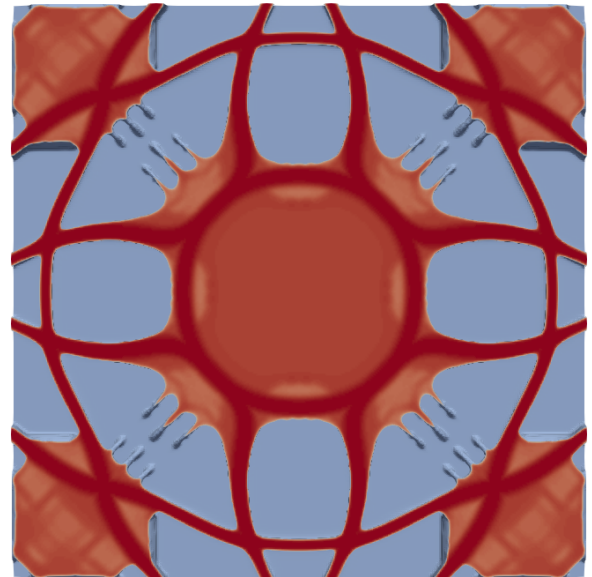


Figure 19: Bottom view of the optimized simply supported slab.

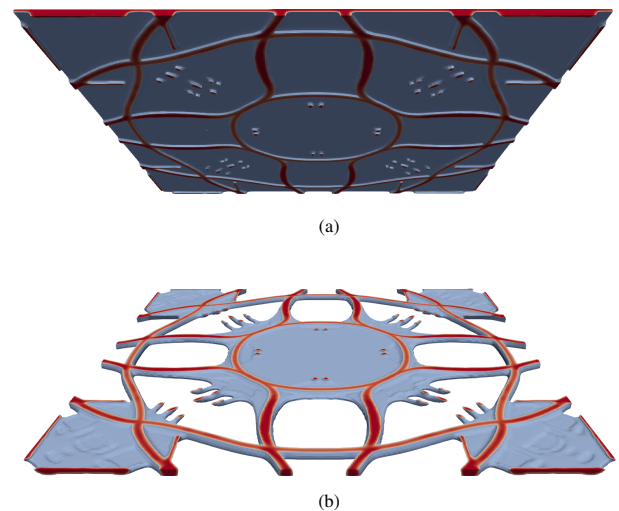


Figure 20: Cross-sectional view at the mid-plane of the simply supported optimized slab, illustrating the connections between its upper and lower parts. (a) Upwards view. (b) Downwards view.

balancing compared to traditional cable layouts that are arranged orthogonally in x and y directions.

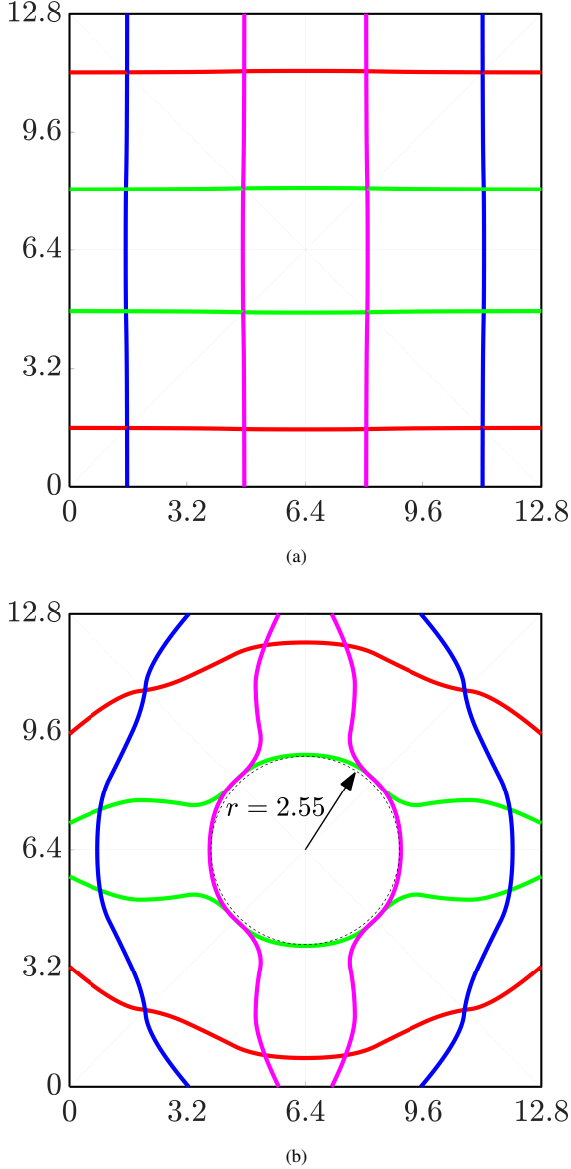


Figure 21: Prestressing cable configurations in the initial and optimized designs of the simply supported slab, where each cable and its symmetric counterpart are marked with the same color. (a) Initial design. (b) Optimized design.

Convergence of the optimization is presented in Figure 22. The graph indicates smooth convergence and fulfillment of the volume constraint. We summarize the values for various measures in both the initial and final designs in Table 4. As expected, and as obtained in previous examples, the displacement component $w_1\phi_1/\phi_1^0$ gradually diminishes during the optimization and approaches a load-balanced design with an optimized value of 0.003. The compliance component of the objective in the optimized design is 0.323, which is derived from a final compliance value of 6.023 kNm . In this design, the maximal displacement of the slab in its intermediate layout is 0.034 m , representing 1/375 of the span.

To further examine the load-balancing effect in the optimized design, we present the vertical displacements at

the upper surface of the slab in Figure 23. As the optimization progresses towards its ideally balanced design, the deflections u_{sd} and u_p (shown in Figures 23a and 23b, respectively) progressively converge to similar absolute values, exhibiting deflections in opposite directions. The combined displacement field, u_{sdp} , is illustrated in Figure 23c. As the optimization progresses, the absolute values of the combined displacements decrease, ideally completely diminishing. When convergence criteria are met, the maximal displacement in u_{sdp} is 0.008 m downwards, and it is located at the center of the slab.

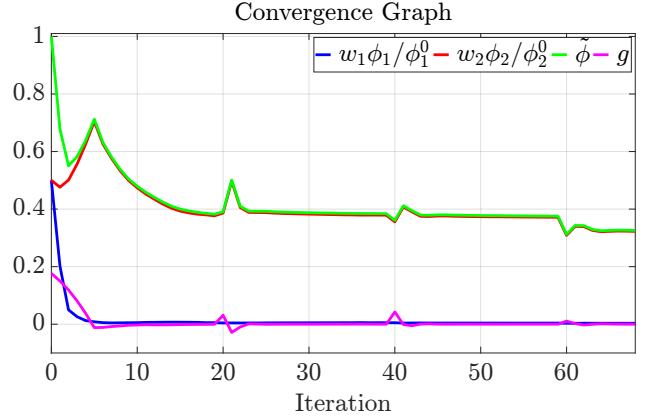
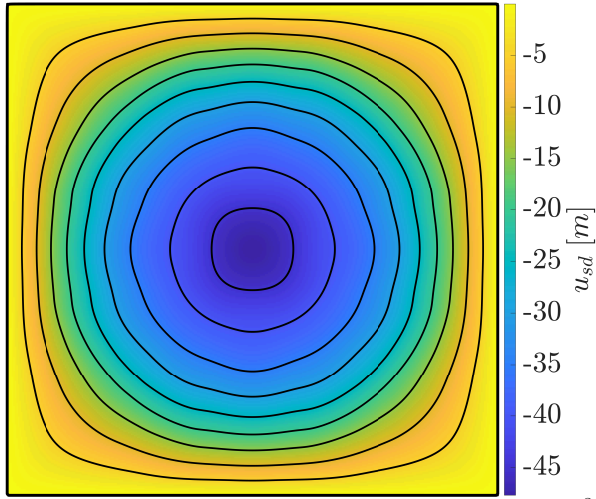


Figure 22: Convergence of the optimization problem, simply supported slab.

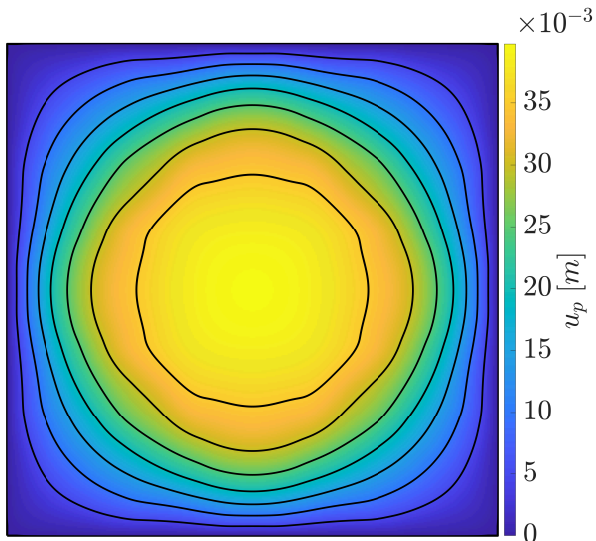
Measure	Initial design	Final design
ϕ_1 [m^2]	22.942	0.150
ϕ_2 [kNm]	9.333	6.023
$w_1\phi_1/\phi_1^0$ [-]	0.5	0.003
$w_2\phi_2/\phi_2^0$ [-]	0.5	0.323
$\tilde{\phi}$ [-]	1	0.326
V_{int} [m^3]	8.648	6.555
g [m^3]	0.177	$-1.3e-4$

Table 4: Optimization of a simply supported slab. Summary of the values for various measures in the initial and final design.

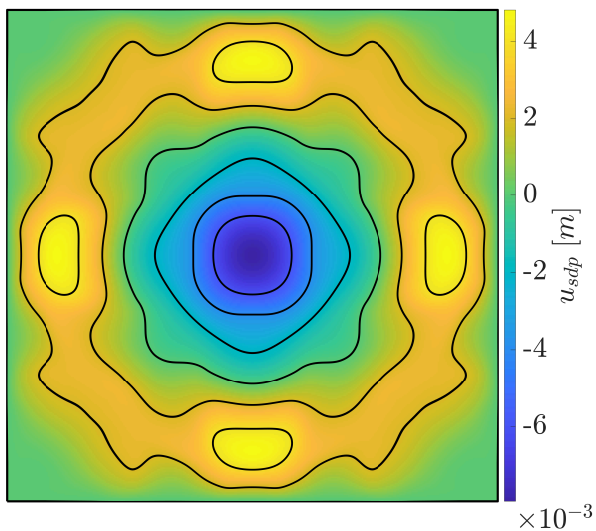
Finally, we wish to evaluate the potential material savings that can be achieved by the simultaneous topology and shape optimization. As before, we find the thickness of a solid slab that has the same compliance ϕ_2 . The required thickness that meets this criterion is found to be roughly 0.23 m . The respective concrete savings are roughly 30%, but one should keep in mind that a thickness of 0.08 m is prescribed at the top of the optimized slab. This restricts the amount of material that can be redistributed via optimization, meaning that the benefit from optimization can exceed 30%. With a hypothetical thickness of 0.23 m , the maximum eccentricity is limited and it is difficult to find a reasonable prestressing force that balances the permanent loads. Nevertheless, similar to the case of the simply supported beam, we can assume that a solid slab will require larger prestressing forces compared to an optimized slab, due to its increased weight and smaller maximal eccentricity.



(a)



(b)



(c)

Figure 23: The vertical displacements at the upper surface of the optimized simply supported slab. From the top: self weight and dead loads; prestressing; and the combination of both.

5.4. Cantilevered slab on columns

In this example, we optimize a slab supported by four internal columns, creating cantilevered regions. The dimensions, external loads, optimization parameters, fixed and merged design variables, as well as all other parameters, remain identical to the previous example, with the sole exception being the column replacing the supported edges. The columns are square-shaped with side lengths of 0.64 m and are positioned near the corners of the slab. Their centers are 1.6 m meters from the slab's edges. Within the column area, the degrees of freedom are constrained in the vertical direction throughout the slab's thickness. As in the previous example, we consider the symmetry of the problem, modeling only one quarter of the slab. The settings of the numerical model are depicted in Figure 24.

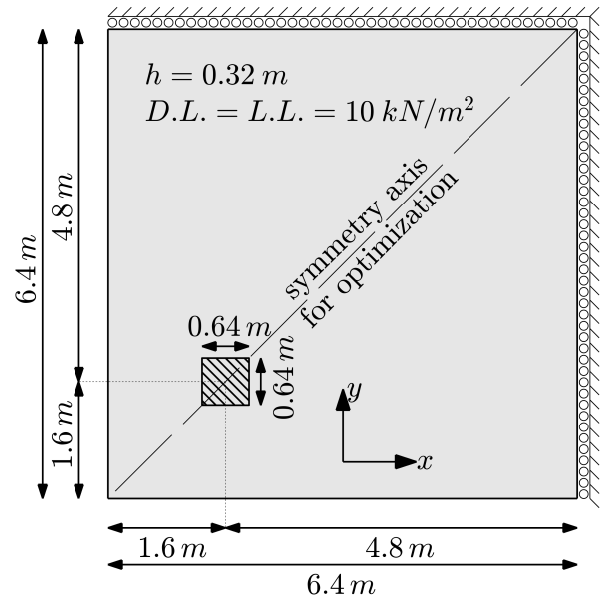


Figure 24: Problem setup for a quarter-symmetric part of a slab supported by columns.

The initial and final designs are presented in Figure 25. A planar view from the bottom is shown in Figure 26. A cross-section at the mid-plane of the slab illustrates the connections between its upper and lower parts, as presented in Figure 27. In the optimized design, a bulk of material is accumulated near the columns, with rib-like parts reinforcing the spans between the columns, forming a stiff column strip that extends across these columns. This design aligns with common strategies in which a stiff column strip is created between columns, creating an internal span of the slab that is supported by the column strips. Additionally, a material region is formed in the bottom part at the center of the slab, enhancing the stiffness of this area where maximal displacement is expected.

The configurations of the cables in both the initial and optimized designs are presented in Figures 28a and 28b, respectively, where each cable and its symmetric counterpart are marked with the same color. The heights of the cables are depicted in Figure 28c. In contrast to the previous example, where all the cables were pushed to their minimum height, Figure 28c illustrates that in this example, the optimization generated cables of varying vertical profile,

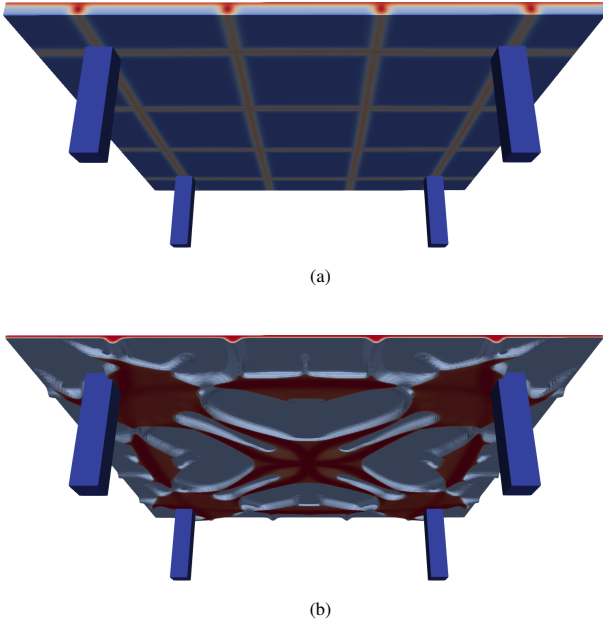


Figure 25: Initial and optimized designs of the slab supported by columns. (a) Initial design with intermediate densities ranging from 0 (blue) to 1 (red). (b) Final design with intermediate densities ranging from 0.5 to 1.

corresponding to the anticipated displacements and tensile forces in each region. The regions outside the column strips behave as cantilevers, hence they are prestressed in their upper part. In contrast, the internal span in the center of the domain is prestressed in its bottom part.

Convergence of the optimization is presented in Figure 29. The optimization is terminated after 67 iterations. In Table 5 we summarize the values of various measures in both the initial and final designs. The optimization process reduced the objective value to 24.1% of its initial value, while also fulfilling the volume constraint. Similar to the previous examples, the optimization progressed towards achieving an ideal balance due to permanent loads, while simultaneously stiffening the design for live loads. Figure 30 shows the vertical displacement fields u_{sd} , u_p and u_{sdp} , as measured over the upper surface of the slab. The balancing effect can be easily observed: prestressing creates a displacement field u_p that has a similar pattern as u_{sd} with opposite sign. The maximal total displacement due to permanent loads is approximately $0.004 m$, at the corners of the slab. We note that both displacement fields $-u_{sd}$ and u_p are downwards at these points. This indicates that the objective function lead the optimizer to balance the displacements mostly at the central span, while the displacements at the cantilevers are not balanced. We presume that this is due to their relatively small area that has minor contribution to the objective.

6. Conclusions

In this paper, we introduced a computational procedure for simultaneous shape and topology optimization of 3D post-tensioned concrete structures. The main contributions of this work that extend the state of the art are as follows:

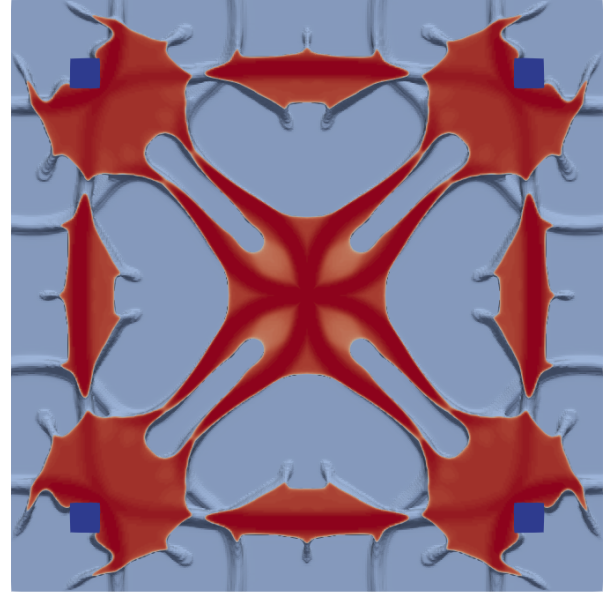


Figure 26: Bottom view of the optimized slab supported by columns.

Measure	Initial design	Final design
$\phi_1 [m^2]$	6.803	0.053
$\phi_2 [kNm]$	4.132	1.959
$w_1 \phi_1 / \phi_1^0 [-]$	0.5	0.004
$w_2 \phi_2 / \phi_2^0 [-]$	0.5	0.237
$\check{\phi} [-]$	1	0.241
$V_{int} [m^3]$	8.648	6.554
$g [m^3]$	0.177	$-2.0e-5$

Table 5: Optimization of a slab supported by columns. Summary of the values for various measures in the initial and final design.

1. A general formulation that can accommodate three-dimensional design scenarios, with complex interactions between the optimized geometries of the concrete and cables;
2. An optimization problem formulation that mimics the design intent of prestressed concrete structures, separating the load-balancing part w.r.t. permanent loads from stiffness maximization w.r.t. live loads;
3. A verification of the optimality of curved cable layouts: previous work (Zelickman and Amir, 2021, 2022) showed optimized spline-based cable layouts with in-plane curvature, where the concrete slabs were modeled as plates. These were explored following the suggested designs of Sarkisian et al. (2018) that were interpreted from density-based topology optimization. Herein, we model the concrete and cables in the most general fashion – as three-dimensional entities – and show that curved layouts indeed emerge;
4. An indication that by combining topology optimization and three-dimensional post-tensioning, material savings of over 30% can be achieved compared to solid members. This strengthens the argument in favor of prestressed concrete for reducing embodied CO₂, suggesting further advantages beyond current knowledge (Miller et al., 2015; Broyles and Hopper, 2023).

The non-traditional layouts presented in Section 5 show-

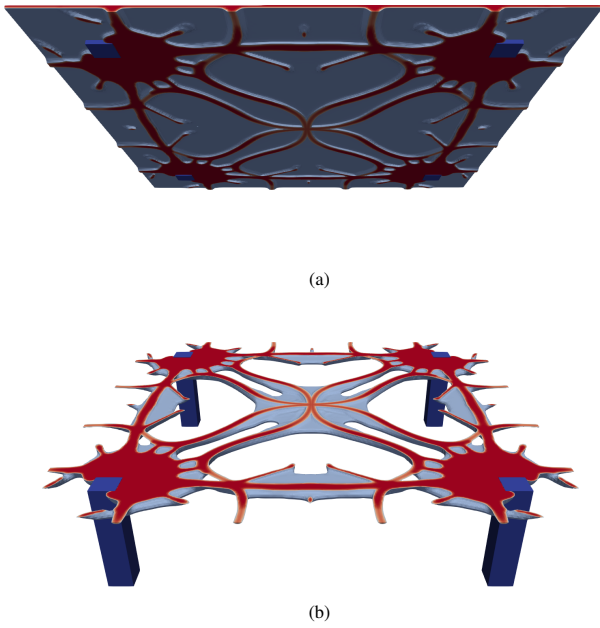


Figure 27: Cross-sectional view at mid-plane of the slab supported by columns, illustrating the connections between its upper and lower parts. (a) Upwards view. (b) Downwards view.

case the potential of the proposed methodology to enable the design of novel, lightweight post-tensioned structures that can be realized by advanced manufacturing processes. Furthermore, the results can provide designers an indication regarding optimal placement of materials, that can be subsequently simplified and adapted to traditional construction methods. Naturally, the methodology is demonstrated through examples of simple, box-shaped domains that can be treated by an academic computer code. Nevertheless, the method is general and applicable to complex geometries, based on standard FEA and spline modeling. To promote extensions and industrial adoption, we provide our complete MATLAB code as supplementary material.

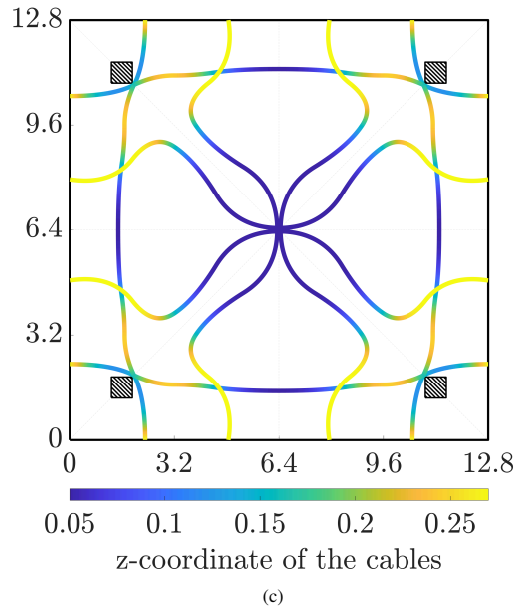
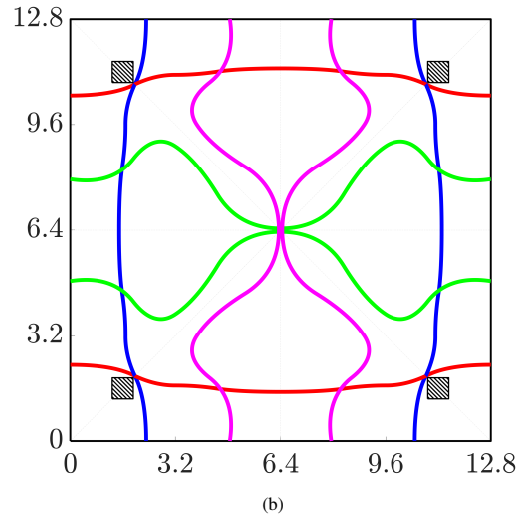
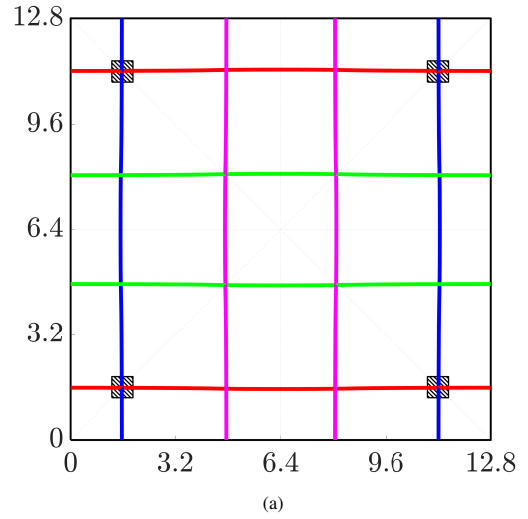


Figure 28: Prestressing cable configurations in the initial and optimized designs of the slab supported by columns. Each cable and its symmetric counterpart are marked with the same color. (a) Initial design. (b) Optimized design.

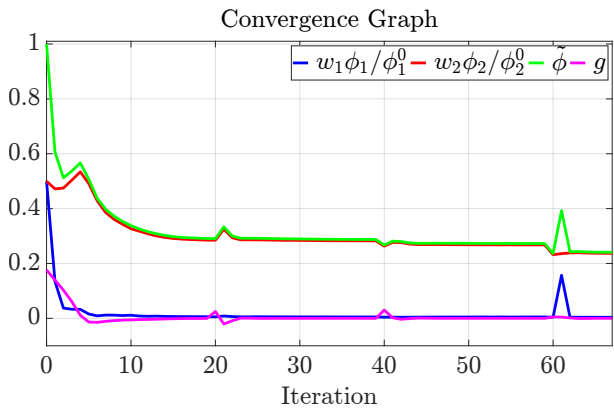
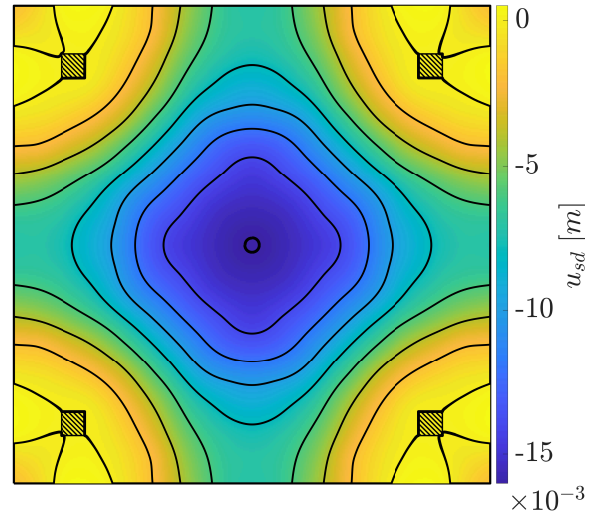
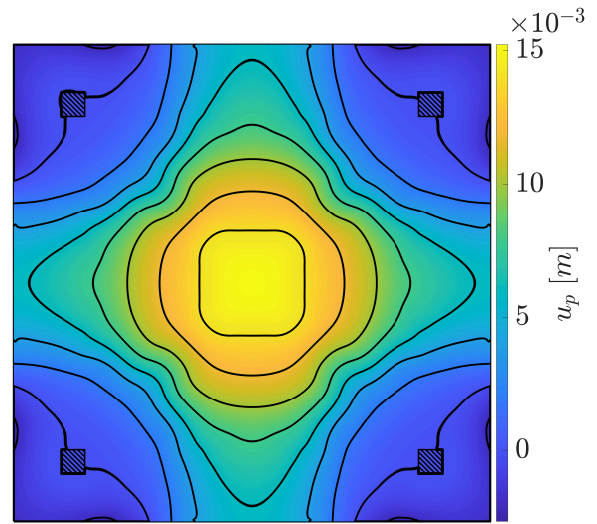


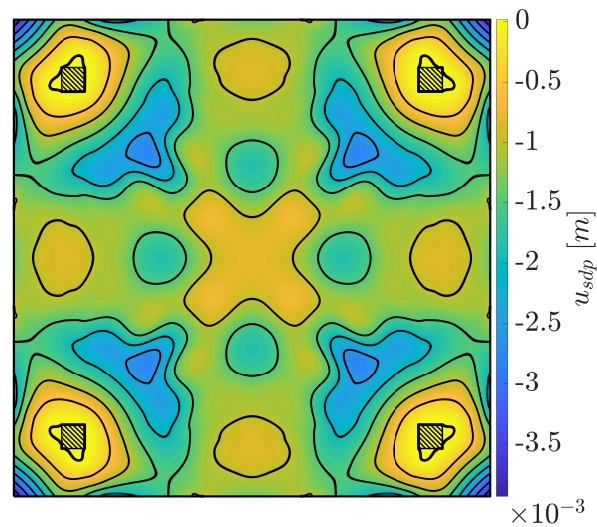
Figure 29: Convergence of the optimization problem, slab supported by columns.



(a)



(b)



(c)

Figure 30: The vertical displacements over the upper surface of the optimized design in the slab supported by columns.

References

- Amir, O., Shakour, E., 2018a. Simultaneous shape and topology optimization of prestressed concrete beams. *Structural and Multidisciplinary Optimization* 57, 1831–1843. Publisher: Springer.
- Amir, O., Shakour, E., 2018b. Topology optimization of post-tensioned concrete beams, in: *Proceedings of IASS Annual Symposia, International Association for Shell and Spatial Structures (IASS)*. pp. 1–8. Issue: 19.
- Andrew, R.M., 2019. Global CO₂ emissions from cement production, 1928–2018. *Earth System Science Data* 11, 1675–1710. Publisher: Copernicus Publications Göttingen, Germany.
- Bendsøe, M.P., 1989. Optimal shape design as a material distribution problem. *Structural optimization* 1, 193–202. Publisher: Springer.
- Bendsøe, M.P., Sigmund, O., 2003. *Topology Optimization - Theory, Methods and Applications*. Springer, Berlin.
- Bourdin, B., 2001. Filters in topology optimization. *International Journal for Numerical Methods in Engineering* 50, 2143–2158.
- Broyles, J.M., Hopper, M.W., 2023. Assessment of the embodied carbon performance of post-tensioned voided concrete plates as a sustainable floor solution in multi-story buildings. *Engineering Structures* 295, 116847. Publisher: Elsevier.
- Bruns, T.E., Tortorelli, D.A., 2001. Topology optimization of non-linear elastic structures and compliant mechanisms. *Computer Methods in Applied Mechanics and Engineering* 190, 3443–3459.
- Guest, J.K., Prévost, J.H., Belytschko, T., 2004. Achieving minimum length scale in topology optimization using nodal design variables and projection functions. *International Journal for Numerical Methods in Engineering* 61, 238–254.
- Jha, I., Pathak, K.K., 2023. Synergetic concrete shape and cable layout optimization of pre-stressed concrete beams. *Structural and Multidisciplinary Optimization* 66, 87. Publisher: Springer.
- Lazarov, B.S., Sigmund, O., 2011. Filters in topology optimization based on Helmholtz-type differential equations. *International Journal for Numerical Methods in Engineering* 86, 765–781. Publisher: Wiley Online Library.
- Lazarov, B.S., Wang, F., Sigmund, O., 2016. Length scale and manufacturability in density-based topology optimization. *Archive of Applied Mechanics* 86, 189–218. Publisher: Springer.
- Li, Y., Wu, H., Xie, X., Zhang, L., Yuan, P.F., Xie, Y.M., 2024. Floatarch: A cable-supported, unreinforced, and re-assemblable 3d-printed concrete structure designed using multi-material topology optimization. *Additive Manufacturing* 81, 104012.
- Miller, D., Doh, J.H., Mulvey, M., 2015. Concrete slab comparison and embodied energy optimisation for alternate design and construction techniques. *Construction and Building Materials* 80, 329–338. Publisher: Elsevier.
- Ooms, T., Vantghem, G., Tao, Y., Bekaert, M., De Schutter, G., Van Tittelboom, K., De Corte, W., 2022. The Production of a Topology-Optimized 3D-Printed Concrete Bridge, in: *RILEM International Conference on Concrete and Digital Fabrication*, Springer. pp. 37–42.
- Sarkisian, M., Long, E., Beghini, A., Garai, R., Shook, D., Henoeh, R., Diaz, A., 2018. Optimal tendon layouts for concrete slabs in buildings derived through density-based topology optimization algorithms, in: *Advances in Structural and Multidisciplinary Optimization: Proceedings of the 12th World Congress of Structural and Multidisciplinary Optimization (WCSMO12)* 12, Springer. pp. 1042–1053.
- Shaked, A., 2023. *Simultaneous Shape and Topology Optimization of Prestressed Structures*. Master's thesis. Faculty of Civil and Environmental Engineering, Technion - Israel Institute of Technology. Haifa, Israel.
- Sigmund, O., Petersson, J., 1998. Numerical instabilities in topology optimization: a survey on procedures dealing with checkerboards, mesh-dependencies and local minima. *Structural optimization* 16, 68–75. Publisher: Springer.
- Sigmund, O., Torquato, S., 1997. Design of materials with extreme thermal expansion using a three-phase topology optimization method. *Journal of the Mechanics and Physics of Solids* 45, 1037–1067.
- Sung, M., Andrawes, B., 2023. Topology Optimization of Continuous Precast Prestressed Concrete Bridge Girders Using Shape Memory Alloys. *Journal of Structural Engineering* 149, 04023051. Publisher: American Society of Civil Engineers.
- Svanberg, K., 1987. The method of moving asymptotes - a new method for structural optimization. *International Journal for Numerical Methods in Engineering* 24, 359–373.
- Vantghem, G., Corte, W.D., Shakour, E., Amir, O., 2020. 3D printing of a post-tensioned concrete girder designed by topology optimization. *Automation in Construction* 112, 103084. URL: <https://www.sciencedirect.com/science/article/pii/S0926580519305096>, doi:<https://doi.org/10.1016/j.autcon.2020.103084>.
- Wallin, M., Ivarsson, N., Amir, O., Tortorelli, D., 2020. Consistent boundary conditions for PDE filter regularization in topology optimization. *Structural and Multidisciplinary Optimization* 62, 1299–1311. Publisher: Springer.
- Wang, F., Lazarov, B.S., Sigmund, O., 2011. On projection methods, convergence and robust formulations in topology optimization. *Structural and Multidisciplinary Optimization* 43, 767–784.
- Wang, Y., Zhang, L., Wang, M.Y., 2016. Length scale control for structural optimization by level sets. *Computer Methods in Applied Mechanics and Engineering* 305, 891–909. Publisher: Elsevier.
- Xu, S., Cai, Y., Cheng, G., 2010. Volume preserving nonlinear density filter based on heaviside functions. *Structural and Multidisciplinary Optimization* 41, 495–505. doi:10.1007/s00158-009-0452-7.
- Zelickman, Y., Amir, O., 2021. Layout optimization of post-tensioned cables in concrete slabs. *Structural and multidisciplinary optimization* 63, 1951–1974. Publisher: Springer.
- Zelickman, Y., Amir, O., 2022. Optimization of post-tensioned concrete slabs for minimum cost. *Engineering Structures* 259, 114132. Publisher: Elsevier.
- Zhang, Z., Yarlagadda, T., Zheng, Y., Jiang, L., Usmani, A., 2021. Isogeometric analysis-based design of post-tensioned concrete beam towards construction-oriented topology optimization. *Structural and Multidisciplinary Optimization* 64, 4237–4253. Publisher: Springer.